A&A, 712, A103 (2026)
https://doi.org/10.1051/0004-6361/202659815
© The Authors 2026

Astronomy & Astrophysics

Magnetar counterparts, kinematics, and birth sites with HST and JWST

A. A. Chrimes[1,2,⋆,⋆⋆], J. D. Lyman[3], A. J. Levan[2,3], A. Borghese[4,⋆⋆], J. H. J. de Bruijne[1], A. S. Fruchter[5], M. G. Guarcello[6], C. Kouveliotou[7,8], N. R. Tanvir[9], and K. Wiersema[10]

[1] European Space Agency (ESA), European Space Research and Technology Centre (ESTEC), Keplerlaan 1, 2201 AZ Noordwijk, The Netherlands
[2] Department of Astrophysics/IMAPP, Radboud University, PO Box 9010, 6500 GL Nijmegen, The Netherlands
[3] Department of Physics, University of Warwick, Gibbet Hill Road, CV4 7AL Coventry, UK
[4] European Space Agency (ESA), European Space Astronomy Centre (ESAC), Camino Bajo del Castillo s/n, 28692, Villanueva de la Cañada Madrid, Spain
[5] Space Telescope Science Institute, 3700 San Martin Drive, Baltimore, MD 21218, USA
[6] Istituto Nazionale di Astrofisica (INAF) – Osservatorio Astronomico di Palermo, Piazza del Parlamento 1, 90134 Palermo, Italy
[7] Department of Physics, The George Washington University, Corcoran Hall, 725 21st St NW, Washington, DC 20052, USA
[8] GWU/Astronomy, Physics and Statistics Institute of Sciences (APSIS), The George Washington University, 725 21st Street NW, Washington, DC 20052, USA
[9] School of Physics and Astronomy, University of Leicester, University Road, Leicester LE1 7RH, UK
[10] Centre for Astrophysics Research, University of Hertfordshire, College Lane, Hatfield AL10 9AB, UK

Received 12 March 2026 / Accepted 20 June 2026

ABSTRACT

Aims. Magnetars are highly magnetised, isolated neutron stars with uncertain formation channels. They comprise a potentially significant fraction of the young neutron star population in the Milky Way and are implicated in the explosion mechanisms of some of the most powerful explosions in nature. We aim to identify magnetars in the near-infrared with *Hubble* Space Telescope (HST) and *James Webb* Space Telescope (JWST) imaging in order to measure their proper motions and search for their birth sites.
Methods. Candidate infrared counterparts were selected based on variability, colours, and proper motions, which are outliers with respect to other sources in the field. Precise proper motions were obtained by tying HST/WCF3 and JWST/NIRcam images to the *Gaia* absolute astrometric reference frame.
Results. We identify new infrared counterpart candidates for PSRJ1622−4950, 1RXSJ 170849.0-400910, and CXOUJ164710.2-455216, representing a substantial increase in the population.
Results. The past trajectory of the 1RXSJ 170849.0-400910-associated source coincides with the supernova remnant G346.6-0.2. The transverse velocity distribution of magnetars is found to be marginally inconsistent with that of young pulsars, due primarily to a dearth of high velocity magnetars. A candidate birth site is identified inside the cone of possible past trajectories in nearly every case. We show, based on the inferred kinematic ages, that magnetar characteristic ages may frequently be lower than the true age but caution that this result depends on the reliability of the birth site associations.
Conclusions. We conclude that magnetars are broadly similar to the wider Galactic neutron star population in terms of their kinematics and birth sites, consistent with magnetar formation being a common outcome of massive star core collapse. However, we find tentative evidence for a dearth of high-velocity magnetars. If real, this may arise from physical differences in the progenitor population giving rise to magnetars or from differences in their post-formation velocity evolution.

Key words. proper motions – stars: kinematics and dynamics – stars: magnetars – stars: neutron – ISM: supernova remnants

1. Introduction

Magnetars are isolated neutron stars with very high magnetic fields, typically 10–100 times stronger than pulsars. Due to their strong fields, they spin down rapidly, and the population within the Milky Way exhibits slow rotation periods $P > 1$ s. Their electromagnetic emission exceeds that expected solely from their spin-down via magnetic braking, given P and $\dot{P}$, and is thought to be additionally powered by the decay of their intense magnetic fields (see e.g. Mereghetti et al. 2015; Turolla et al. 2015; Kaspi & Beloborodov 2017; Esposito et al. 2021; Igoshev et al. 2021, for reviews). They have young characteristic ages of $<10^5$ yr, as inferred from P and $\dot{P}$ under the assumption of magnetic braking, a constant dipolar field, and braking index $n = 3$ (e.g. Hamil et al. 2015). Approximately 30 have been directly observed, predominantly in the plane of the Milky Way, plus a few in the Magellanic Clouds (Olausen & Kaspi 2014).

Most known magnetars have thus far been discovered through high-energy outbursts (Coti Zelati et al. 2018) or flares (e.g. Mazets et al. 1979; Kouveliotou et al. 1999; Palmer et al. 2005; Negro et al. 2024), some of which can be luminous enough to be detected over extragalactic distances (Burns et al. 2021; Mereghetti et al. 2024). Historically, magnetars were labelled as anomalous X-ray pulsars (AXPs) or soft gamma repeaters (SGRs) based on their observational properties, but are now understood to be manifestations of the same physical objects (e.g. van Paradijs et al. 1995; Thompson & Duncan 1996; Kouveliotou et al. 1998).

⋆ Corresponding author: ashley.chrimes@esa.int
⋆⋆ ESA Research Fellows.

Open Access article, published by EDP Sciences, under the terms of the Creative Commons Attribution License (https://creativecommons.org/licenses/by/4.0), which permits unrestricted use, distribution, and reproduction in any medium, provided the original work is properly cited.
This article is published in open access under the Subscribe to Open model. Subscribe to A&A to support open access publication.

Follow-up observations of Galactic magnetars often reveal multi-wavelength counterparts, ranging from ubiquitous quiescent X-ray emission to several optical–infrared counterparts (e.g. Tam et al. 2004; Morii et al. 2005; Testa et al. 2008; Dhillon et al. 2011; Levan et al. 2018) and a handful of radio detections (Camilo et al. 2006, 2008; Levin et al. 2010; Shannon & Johnston 2013; Esposito et al. 2020). Magnetars are known to be variable at X-ray and optical/near-infrared (NIR) wavelengths. In some cases variations in the NIR flux appear to correlate with X-ray activity (e.g. Kern & Martin 2002; Tam et al. 2004; Israel et al. 2005; Dhillon et al. 2005; Chrimes et al. 2025), while in others, not (e.g. Durant & van Kerkwijk 2005, 2006b; Lyman et al. 2022). This variability is in any case a useful tool for identifying NIR counterparts. Given crowded sight-lines in the Galactic plane and relatively large positional uncertainties from X-ray observations, identifying if one of a number of NIR candidates is variable is an effective way to unambiguously identify the counterpart (e.g. Israel et al. 2002, 2005).

Magnetars are also typically redder than field stars at NIR wavelengths (e.g. Chrimes et al. 2022b). The optical-IR flux is likely non-thermal and magnetospheric in origin (e.g. Mignani et al. 2007), given the correlation with X-ray emission seen in some cases and the power-law spectral energy distribution (SED) seen in 4U0142+61 (Muñoz-Darias et al. 2016; Hare et al. 2024). However, this object appears spectrally variable on a timescale of years and was previously observed to have an NIR bump in the SED consistent with blackbody emission from a debris disc (Wang et al. 2006; Ertan et al. 2007).

Magnetars are often kinematically distinct with respect to the objects in the surrounding field (e.g. Helfand et al. 2007; Tendulkar et al. 2012, 2013). As neutron stars, they have likely received large natal kicks imparting velocities that are much greater than the velocity dispersion and bulk motion of field stars (e.g. Hobbs et al. 2005; Verbunt et al. 2017; Igoshev 2020; Disberg et al. 2024; Disberg & Mandel 2025). Determining the proper motions of magnetars, and hence their transverse velocities if a distance can be measured or estimated, allows us to determine their natal kick distribution and, ultimately, their birth sites by tracing back their motion. This is possible thanks to their young ages. There are several examples of magnetars associated with supernova remnants (SNRs) and stellar clusters (e.g. Muno et al. 2006; Gelfand & Gaensler 2007; Anderson et al. 2012; Lyman et al. 2022); the latter also enables progenitor mass estimates based on cluster age (Davies et al. 2009; Ritchie et al. 2010).

According to the literature, magnetars obtained their extreme magnetic fields either through magnetic flux conservation during the core-collapse process (the 'fossil field' hypothesis, Woltjer 1964; Ferrario & Wickramasinghe 2006; Schneider et al. 2020) or through a dynamo upon neutron star formation (Thompson & Duncan 1993; Obergaulinger et al. 2014; Mösta et al. 2015; White et al. 2022; Reboul-Salze et al. 2022). The recent discovery of a Wolf-Rayet star with a magnetic field strong enough for magnetar formation suggests that the inherited fossil field scenario is plausible (Shenar et al. 2023), while the explanation of some high-energy extragalactic transients with (millisecond) magnetar central engines (e.g. gamma-ray bursts and super-luminous supernovae; Gompertz et al. 2014; Metzger et al. 2015; Omand & Sarin 2024; Mukhopadhyay & Kimura 2025) favours their rapid rotation at birth. However, there is no evidence of additional energy injection into the SNRs surrounding Galactic magnetars due to the post-birth spin down of a rapidly rotating neutron star (Vink & Kuiper 2006). Indeed, population synthesis studies suggest that the population of Galactic magnetars were likely not born with sufficient rotational energy to power such high-energy transients (Rea et al. 2015). It is notable that not every Galactic magnetar has a clear SNR or cluster association (e.g. Tendulkar et al. 2013; Chrimes et al. 2025), despite their young characteristic (spin-down) ages.

Another class of transients linked with magnetars are fast radio bursts (FRBs), particularly following the detection of FRBs from the Galactic magnetar SGR1935+2154 (CHIME/FRB Collaboration 2020; Bochenek et al. 2020). If the FRB-magnetar association is universal, the subsequent discovery of FRBs in a globular cluster (Kirsten et al. 2022) and ancient elliptical galaxies (Sharma et al. 2023) may point towards some fraction of magnetar formation through non-core-collapse channels with long delay times, such as the accretion- or merger-induced collapse of white dwarfs (Nomoto & Kondo 1991; Levan et al. 2006; Margalit et al. 2019).

Magnetar velocities and birth sites can be compared with the wider (young) neutron star population. In this way we can discern differences in their progenitor systems, if any (e.g. Hu & Zhang 2026). High resolution NIR imaging is ideally suited for this task. Measuring proper motions with even the highest resolution X-ray imaging is challenging (but possible for high proper motion objects or over long baselines, Kaplan et al. 2009; Rigoselli et al. 2024), and only a handful of Galactic magnetars are radio-bright (and hence amenable to radio interferometry; Helfand et al. 2007; Deller et al. 2012; Ding et al. 2020, 2024). Efforts have successfully been made with ground-based NIR observations assisted by adaptive optics (Tendulkar et al. 2012, 2013), but challenging absolute astrometry and the sensitivity of such observations is a limitation.

In this work, we identified NIR magnetar counterparts in repeat *Hubble* Space Telescope (HST) imaging by searching for red, variable, and kinematically distinct sources consistent with magnetar X-ray localisations. In one case, these observations were supplemented by *James Webb* Space Telescope (JWST) imaging. By measuring the proper motions of magnetar NIR counterparts with respect to previous imaging, new constraints on the velocity distribution, birth sites, and kinematic ages of several Galactic magnetars were obtained.

The paper is structured as follows. In Sect. 2 we describe the HST and JWST data used, the data reduction, and the magnetars in our sample. Section 3 outlines in the methodology including photometry, astrometry, proper motion measurement, and counterpart identification. Section 4 presents the results including three new magnetar counterparts, transverse velocities, and birth site identifications. A discussion and conclusions follow in Sects. 5 and 6. Magnitudes are reported throughout in the AB system (Oke & Gunn 1983), and uncertainties are stated at the 1σ confidence level unless otherwise stated.

2. Observations and data reduction

2.1. Hubble Space Telescope

The new HST observations used in this work (programme GO 17927, PI: Chrimes) are summarised in Table A.1 of the Appendix. All observations were taken with the Wide Field Camera 3 (WFC3 Kimble et al. 2008), and each observation consists of either three or four dithered exposures. The sample comprises 15 magnetars for which at least one candidate counterpart was identified in previous HST observations (Chrimes et al. 2022b). Also listed are any previous epochs of HST

observations, the filters used, and the programme IDs of those observations. We reduced the data following standard ASTRODRIZZLE procedures (Fruchter & Hook 2002)[1], including corrections for geometric distortion. The calibrated _FLT files for each image, which underwent flat fielding and dark subtraction, were drizzled with a final orientation north up, east left, a PIXFRAC of 0.8 and a final pixel scale of 0.065 arsec pixel^{-1}.

2.2. JWST

Two objects in our sample were imaged with JWST: 4U0142, as part of a campaign specifically designed to study the magnetar, and CXOUJ1647, whose location was covered by JWST imaging of the Westerlund 1 stellar cluster (Guarcello et al. 2025). A detailed JWST study of 4U0142 has already been published by Hare et al. (2024). However, as the observations were taken with the SUB400P sub-array, the field of view is small, and there are no reference sources we can use for astrometry (and hence a proper motion measurement) in the images.

CXOUJ1647 on the other hand was imaged as part of a large mosaic covering the Westerlund 1 cluster (programme GO 1905, PI: Guarcello). For this magnetar we have two previous epochs of F140W HST imaging, a 2026 epoch of F125W and F160W, plus imaging in eight JWST wide filters (five NIRcam and three MIRI, all obtained in 2023). We used the NIRcam/F150W image for the proper motion measurements and the DOLPHOT catalogue produced by Guarcello et al. (2025, see the next section)[2].

2.3. Sample summary

Our final sample consists of 14 objects with at least two epochs of space-based imaging. These are the 15 objects listed in Table A.1, excluding SGR1806 whose 2025 epoch consists of the first set of HST images for this object. All remaining objects have two HST epochs (taken in 2018, 2020, and 2025), except for SGR0501 (three epochs of HST between 2010 and 2025), SGR1935 (five epochs of HST between 2015 and 2025), and CXOUJ1647 (four epochs, $3\times$HST, and $1\times$JWST spanning 2017–2026).

In Fig. 1 (continued in Fig. A.1) we show image cutouts ('stamps') around the position of each magnetar. The approximate 3σ X-ray error circle is plotted in each case (assuming Gaussian uncertainties and based on positions reported in the McGill magnetar catalogue, Olausen & Kaspi 2014, we note that none of the 14 objects in our sample have a position measured with radio interferometry)[3]. Sources, which we identify as NIR counterparts to magnetars based on the criteria outlined in the next section, are circled in red.

3. Methodology

3.1. Photometry

We carried out source detection and photometry for all HST images using DOLPHOT (Dolphin 2000, 2016; Weisz et al. 2024)[4] using the point spread functions of Anderson (2016). The detection thresholds for point sources were set at 3σ. Source detection was performed using only the individual _FLT frames, with photometry of detected sources performed on both these and the drizzled _DRZ images. Magnitudes were converted to the AB system using conversions calculated with STSYNPHOT[5]. These conversions (added to Vega magnitudes to obtain AB) are 0.9204 (F125W), 1.0973 (F140W), 1.2277 (F150W), and 1.2741 (F160W). For the JWST observations of CXOUJ1647, we used the existing DOLPHOT output catalogue of sources in and around Westerlund 1 produced by Guarcello et al. (2025), as described in that paper. Additions to the JWST/NIRcam Vega magnitudes are 0.7949 (F115W), 1.2277(F150W), 1.7014 (F200W), 2.3160 (F277W), and 4.3664 (F444W) (Rodrigo & Solano 2020)[6].

3.2. Astrometry and proper motions

By measuring the relative offset of a source in images taken some time apart, with respect to the surrounding objects in the field, we can measure its proper motion. We adopted a method described in detail by Bedin & Fontanive (2018) and Lyman et al. (2022) but briefly summarise it here. Starting from the DOLPHOT source catalogues, we first performed quality cuts (removing objects, which are not point sources or are overly crowded, as outlined by Lyman et al. 2022). *Gaia* sources within the HST/WFC3 field of view were then selected (using *Gaia* data release 3, Gaia Collaboration 2023), and sources with a poor astrometric solution (a renomalised unit weight error, or RUWE > 1.2, Penoyre et al. 2022) were removed. The *Gaia* positions were then offset, using their proper motions where available, to obtain their expected positions at the time of each HST observation. These shifted positions (in equatorial coordinates) were then transformed first into a tangent plane and then to HST pixel (x,y) coordinates, using the existing world coordinate system of the images (which itself has been determined through an astrometric tie with *Gaia*). The x,y coordinates of the shifted *Gaia* sources were then matched with the HST source catalogues by identifying the closest match to each *Gaia* source. Outliers in the resulting offset distribution for the matching pairs (above the 95$^{\text{th}}$ percentile) were rejected. A new (x,y) to ($\alpha\cos(\delta)$, δ) transformation was then fitted following Bedin & Fontanive (2018), where the uncertainty in this transformation represents the absolute astrometric uncertainty.

This method yields absolute astrometry at a comparable level to HST-only relative astrometry (typically several tens of milliarcseconds, Lyman et al. 2022). The uncertainty on the resulting proper motion of a given source has contributions from both the absolute astrometric uncertainty and the positional uncertainty of the source (i.e. how well its centroid can be measured, which is proportional to the signal-to-noise). Because we have DOLPHOT catalogues containing positions for all sources in the images above a detection threshold, we can plot, for any pair of images, the difference in Right Ascension (RA) $\Delta\alpha\cos(\delta)$ and Declination (Dec) $\Delta\delta$ between sources, which are detected in both images. This is shown in Fig. 2 and Figs. B.1, B.2, B.3, B.4 of the Appendix. In some cases we compared the positions of objects in images taken just minutes apart (e.g. two images with different filters in the same HST orbit). In these cases, the scatter is centred on 0,0 and simply reflects the astrometric uncertainties. When the images are taken several years apart, the bulk motion of stars in the field is evident as a shift in the clouds of points. This apparent bulk motion can arise from both the differential rotation between our position in the Galaxy, along

[1] Available via DRIZZLEPAC, at php https://www.stsci.edu/scientific-community/software/drizzlepac
[2] The data described here may be obtained from https://dx.doi.org/10.17909/f9d0-er88
[3] https://www.physics.mcgill.ca/~pulsar/magnetar/main.html
[4] http://americano.dolphinsim.com/dolphot/
[5] https://github.com/spacetelescope/stsynphot_refactor
[6] The SVO filter profile service.

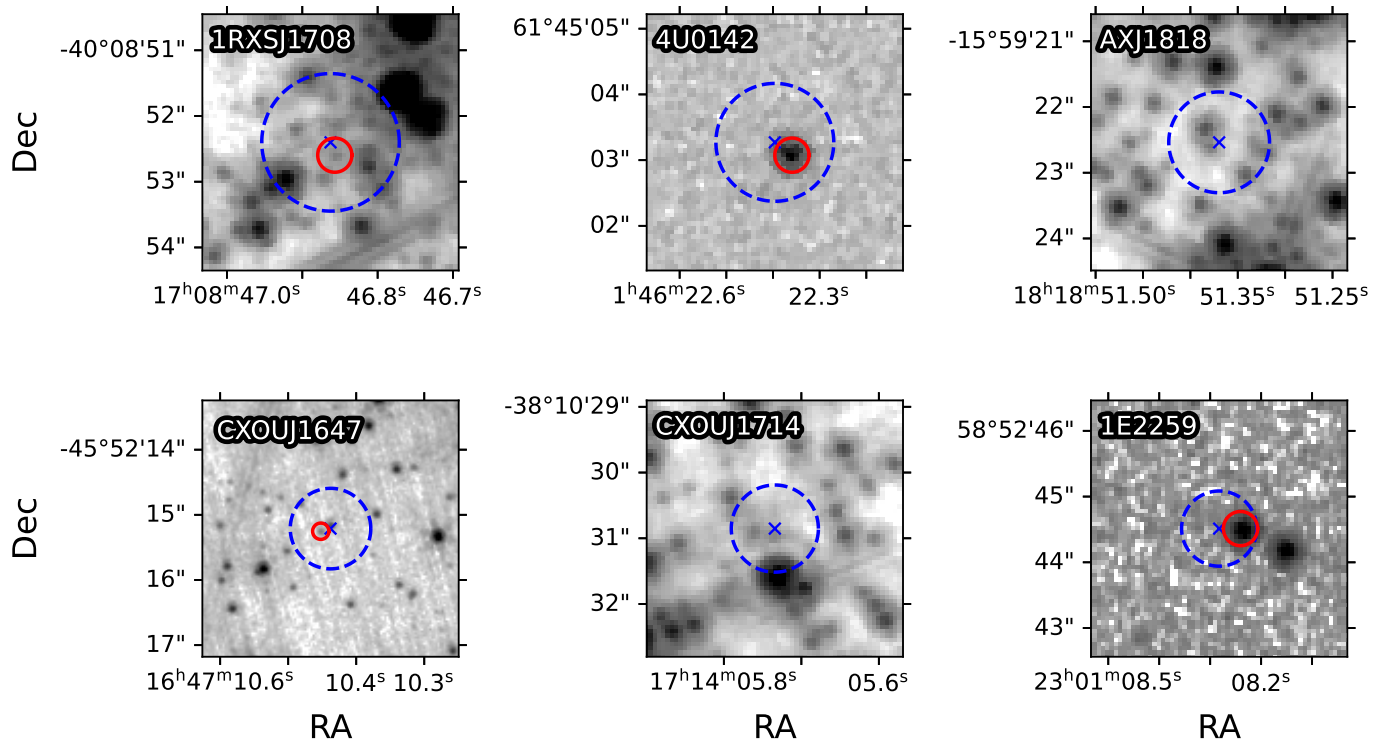


Fig. 1. HST cutouts with the magnetar 3σ X-ray localisations indicated by the dashed blue circles with a cross at the centre (from Olausen & Kaspi 2014, and references therein). If an NIR counterpart candidate is identified, its position is indicated by a red circle. Only the latest (2025 epoch) F160W images are shown, with the exception of CXOUJ1647 (a 2023 JWST/NIRcam F150W image). Each cutout measures 4×4 arcsec, and they are oriented north up, east left. This is continued in Fig. A.1 of the Appendix.

the sight-line in question, and the 'real' motion of stars in their Local Standard of Rest (LSR; e.g. moving groups). When reporting proper motions in Sect. 4, we first accounted for differential rotation (and Solar velocity with respect to the LSR; Ding et al. 2019) following Verbunt et al. (2017), Lyman et al. (2022). The reported values therefore represent proper motions relative to the LSR at the assumed distance of the magnetar (see Table 2), i.e. they are peculiar proper motions. The impact of the large distance and hence velocity uncertainties are explored in Sect. 5).

3.3. Counterpart identification

To identify NIR counterparts, we followed an established methodology of searching for objects in the magnetar X-ray error circles, which are discrepant from objects in the field in terms of proper motion, colour, and variability. This is particularly useful in crowded fields with multiple candidates, and because magnetars are faint (and potentially undetected) at these wavelengths. In most cases we have two HST epochs, with F125W and F160W imaging in each. In Figs. 2, B.1, B.2, B.3, and B.4, we plot the positional shifts ($\Delta\alpha\cos(\delta)$, $\Delta\delta$) for all NIR sources in the field, which are matched between the images. A matching radius of 75 mas was used, which is indicated in these figures by dashed grey circles. This radius was extended for objects inside the X-ray error circles to enable the identification of high proper motion objects; this point is discussed in further detail in Sect. 5. In the standard case, we have one panel where the two images are taken minutes apart (same epoch, different filters). In these panels, the colour map represents the F125W-F160W colour, and the $\Delta\alpha\cos(\delta)$, $\Delta\delta$ scatter solely reflects astrometric noise. We also have panels showing $\Delta\alpha\cos(\delta)$, $\Delta\delta$ for pairs of F125W and F160W images, obtained years apart. Here, the colour scale represents variability instead (i.e. Δ F125W, Δ F160W), and the distribution in $\Delta\alpha\cos(\delta)$, $\Delta\delta$ parameter space has contributions from both astrometric noise and proper motion as described in the previous section.

In every panel of these figures, objects inside the 3σ X-ray error circles are indicated with bold outlines, and the best counterpart candidate based on proper motion, colour, and variability is marked with a triangle. To classify an object as a counterpart candidate, we required either (i) at least one of proper motion, colour, or variability to be a $>3\sigma$ outlier relative to the scatter in the field objects in at least one epoch, or (ii) two or more of proper motion, colour, or variability to be $>2\sigma$ outliers. Figures 2, B.1 and B.2 show the magnetars where a kinematically distinct, red and/or variable object was found in the X-ray error circle. If distinct from this candidate, the highest probability source based on the chance alignment probability (P_{chance}; e.g. Chrimes et al. 2022b) is marked with a pentagon. We note that in each case where there is more than one candidate in the error circle, our preferred candidate is not the one with the lowest P_{chance}. This demonstrates that P_{chance} is not an effective selection method for magnetar counterparts, perhaps not surprising given that their faint magnitudes, and the nature of the P_{chance} selection, which favours brighter objects. All markers follow the same colour-mapping as the cloud of field sources.

Six objects in our sample meet one of the proper motion, colour, or variability criteria: 4U0142 and 1RXSJ 1708 pass purely on their discrepant proper motion; SGR1935 passes on variability alone; SGR0501 and PSRJ1622 pass on both proper motion and variability; and 1E2259 passes on all three criteria. In every case the parameter on which the selection is made exceeds

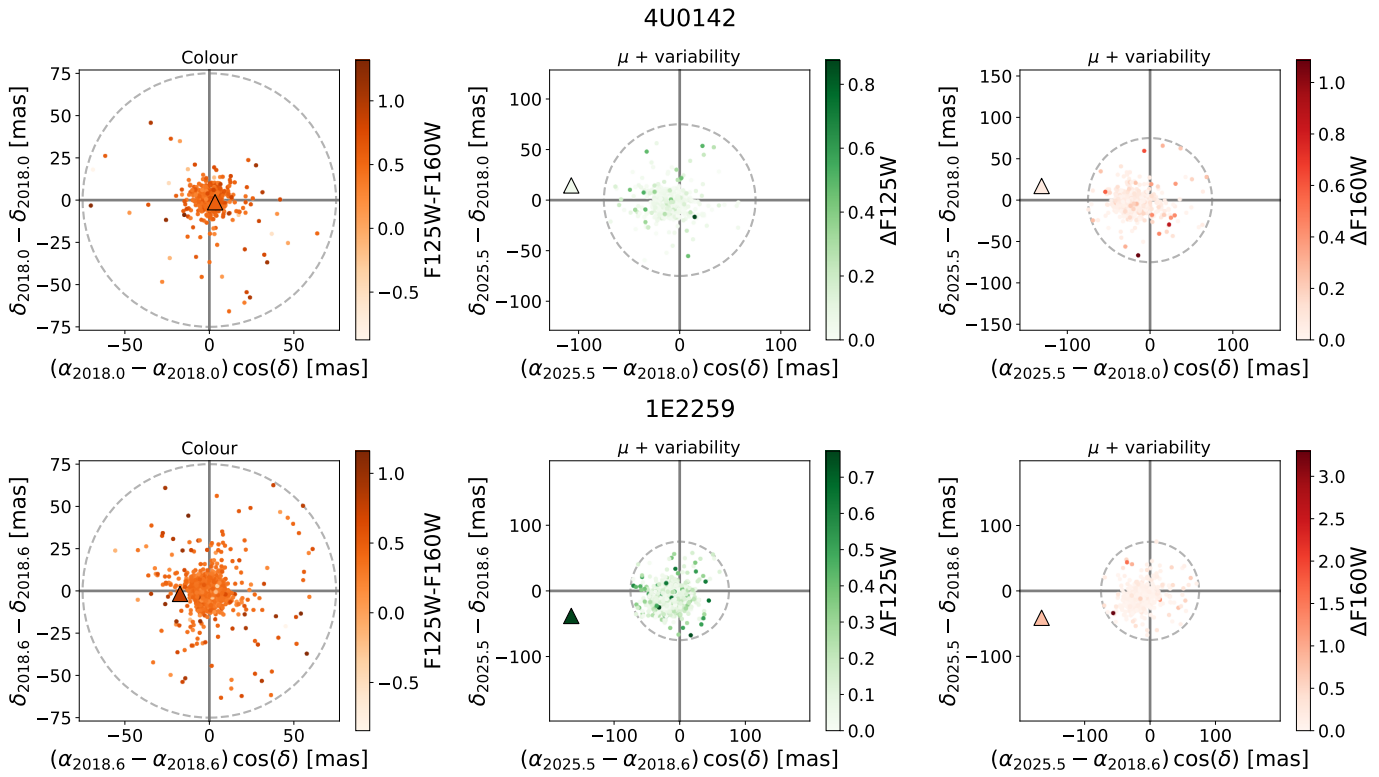


Fig. 2. Figures showing the change in Right Ascension and Declination of sources in the HST images between epochs. These include cases where a good counterpart candidate was identified within the 3σ X-ray error circles shown in Figs. 1 and A.1, based on distinct kinematics, colour, and/or variability, and for which four images were available (two filters in two epochs). In each case, our preferred counterpart candidate is labelled with a triangle. The best candidate in the 3σ X-ray error region per the P_{chance} criteria is marked with a pentagon (if different from our favoured counterpart; see also Chrimes et al. 2022b). The lowest P_{chance} values in each case are (top to bottom) $<10^{-3}$, 0.016, 0.043, and 0.164. Other objects in the X-ray localisation region are labelled as circles with bold outlines, with the colouring of all markers following the same mapping as the cloud of field sources. Left column: Comparison of source positions in images taken minutes apart, showing the level of astrometric noise. The points correspond to the objects detected in the two HST images and are colour-coded according to their F125W-F160W colour. Middle: Movement of sources between the first and second epochs of F125W imaging. The bulk motion of sources in the field is clear. The magnetars are offset from this systemic drift due to their natal kicks. The points are colour-coded according to the difference in F125W magnitude between the epochs. Right: As in the middle panels but showing the difference between the two epochs in F160W. The dashed grey circles represent the matching radius (75 mas) used to identify common sources between each pair of images. This is continued in Figs. B.1, B.2, B.3, and B.4 of the Appendix.

3σ. Of these, the counterparts of 4U0142, 1E2259, SGR0501, and SGR1935 were already known, further supporting the validity of the method. We additionally report new NIR counterparts for PSRJ1622 and 1RXSJ 1708.

4U0142, 1E2259, PSRJ1622, and 1RXSJ 1708 have just two epochs of two-filter HST imaging. SGR0501 has four epochs of observation, the first two solely in F160W and last two in both F125W and F160W. Using the 2025 epoch as the reference, we therefore have three $\Delta F160W$, one $\Delta F125W$, and one F125W-F160W as the possible combinations. For brevity in Fig. B.2 we only show F125W-F160W, ΔF125W, and the ΔF160W with the longest temporal baseline. The known counterpart of SGR0501 clearly stands out in terms of kinematics and variability. SGR1935 has five epochs: four in which the sole filter was F140W and one in 2025 with F125W and F160W. In Fig. B.2 we show the 2025 F125W-F160W colour, the ΔF140W with the longest baseline, and finally a comparison between F125W (2026) and F140W (2017). The last panel represents the largest temporal baseline available for this object, but we cannot disentangle colour and variability when comparing different filters taken years apart, so no colour-mapping is applied. The proper motion of SGR1935 is clearly visible, particularly in this final panel.

The rest of the sample is shown in Figs. B.3 and B.4 in the Appendix. In these cases, none of the sources in the X-ray localisation meets the selection criteria, so we cannot confidently claim to have identified the counterpart. The 'best candidate' in Figs. B.3 and B.4 is labelled as such purely on the chance alignment probability (i.e. they are the brightest sources in the error circle).

4. Results

We present the apparent magnitudes, fluxes, colours and variability of confirmed or preferred counterparts in Table 1, and LSR-corrected proper motions for the six counterparts in Table 2. The latter also includes distance estimates for the magnetars and the resulting peculiar transverse velocities v_t at that distance. Notes on individual objects – for which we report a new counterpart candidate, fail to recover a previously known counterpart, or successfully 're-discover' a known source – are provided in the following subsections.

These results bring the total number of magnetar IR counterparts to eleven (two of which are newly reported here) out of ∼30 known (Rea & De Grandis 2026). Six magnetars with IR counterparts are shown in Figs. 2, B.1, and B.2, along with SGRs 1806 and 1900 (Kosugi et al. 2005; Tendulkar et al. 2012), 1E1048.1-5937 (Tam et al. 2008), XTEJ1810-197, and 1E1841-045 (Testa et al. 2008)

4.1. Recovered known counterparts

We successfully recover the known NIR counterparts of 1E2259 (Hulleman et al. 2001; Tam et al. 2004; Tendulkar et al. 2013), 4U0142 (Hulleman et al. 2004; Wang et al. 2006; Hare et al. 2024), SGR1935 (Levan et al. 2018; Lyman et al. 2022), and SGR0501 (Dhillon et al. 2011; Chrimes et al. 2025). These objects all have a previously measured proper motion, which are provided for reference in Table 2, and we reduced the uncertainties further by moving to space-based observations and/or extending the temporal baseline.

4.2. Unrecovered known counterparts

4.2.1. SGR1806-20

The 2025 epoch imaging presented in this paper is the first space-based imaging of SGR1806, although a magnitude 23–34, variable K_s-band counterpart was identified by Israel et al. (2005), Kosugi et al. (2005) and subsequently in ground-based Very Large Telescope (VLT) and Keck imaging Tendulkar et al. (2012). There is no detected source at the position of the source labelled A by Israel et al. (2005), Tendulkar et al. (2012) in the 2025 F125W and F160W images. There is however a slightly offset source present in the F160W images (the closest in terms of wavelength). This source lies between the position of SGR1806 in 2004 and the star to the south-west, which Israel et al. (2005), Tendulkar et al. (2012) labelled C. Assuming this is SGR1806 and comparing its position with the reported 2004 coordinates, it would have a proper motion of $\sim$10 mas yr^{-1}, higher than the value of $\sim$5 mas yr^{-1} reported by Tendulkar et al. (2012) and in an approximately perpendicular direction. We therefore assume that the F160W source is unrelated and that SGR1806 is undetected in our F125W and F160W imaging. The high extinction along the sight-line means that our imaging, even in the longer F160W filter, could reduce the counterpart flux as much as 6 magnitudes (for a flat spectrum and $A_V \sim 30$; Eikenberry et al. 2004) versus the 23–34 K_s-band magnitude, plausibly explaining our non-detection.

4.2.2. SGR1900+14

The infrared counterpart of SGR1900 was previously identified in VLT/NACO (Testa et al. 2008) and Keck/NIRC2 (Tendulkar et al. 2012) K_s-band imaging, using adaptive optics for enhanced spatial resolution, which reached the approximate milli-arcsecond level. Comparing the images in those papers with Figs. 1 and A.1, we can see that the source remains undetected in our imaging. This is likely due to the factor of $\sim$10 lower spatial resolution and subsequent blending with the adjacent star, rather than variability, given that our HST imaging has a limiting magnitude, which is 5–6 magnitudes deeper. Higher resolution observations with current adaptive-optics-assisted ground-based facilities, JWST, or future observatories such as the European Extremely Large Telescope (Gilmozzi & Spyromilio 2007) would likely be required to re-detect the counterpart. In any case, this magnetar already has a proper motion measurement (Tendulkar et al. 2012, see Table 2).

4.3. New counterpart candidates

4.3.1. PSRJ1622−4950

We report the discovery of a candidate infrared counterpart to PSRJ1622−4950. The object is one of four detected in the 3σ X-ray error circle. It is kinematically distinct with a high proper motion and shows variability (most notably in F160W). This is not the candidate identified by Chrimes et al. (2022b), which was simply selected based on P_{chance} arguments.

Levin et al. (2010) reported a distance for PSRJ1622−4950 (and the associated SNR G333.9+0.0) of $\sim$9 kpc (with an uncertainty of a factor of $\sim$2), based solely on the radio dispersion measure using the NE2001 electron density model (Cordes & Lazio 2002). Placing the IR counterpart of PSRJ1622−4950 at 9 kpc and correcting for the extinction at 1.6 μm of 5.2 magnitudes (adopting a Fitzpatrick extinction law, Fitzpatrick 1999, and $R_V = 3.1$), we find the source to be extremely blue, with an intrinsic absolute magnitude of $M_{F160W} \sim 3.5$. This is $\sim$5–8 magnitudes brighter than other confirmed IR counterparts (e.g. Chrimes et al. 2022a). Placing it instead at 5.5 kpc, the distance implied by the YMW16 electron density model (Yao et al. 2017), and adopting approximately half the extinction as implied from the A_V-NH relation (Predehl & Schmitt 1995), we find $M_{F160W} \sim 8$, which is more comparable with other counterparts. Overall, a distance of $\sim$5 kpc brings PSRJ1622−4950 into line with the rest of the population, and given the large uncertainty on the previous distance estimate, such a revision is plausible. We therefore suggest that this object (and its associated SNR) lie at $\sim$5 kpc, adopting this revised distance throughout. Given the NIR luminosity this implies ($\sim 5 \times 10^{31}$ erg s^{-1}), the IR efficiency for this magnetar, defined as $\log_{10}(L_{IR}/\dot{E})$ (Rea et al. 2010), is –2.2, where we have adopted $\dot{E} = 8.5 \times 10^{33}$ erg s^{-1} (Levin et al. 2010). Previous measurements for magnetars have yielded values in range –4 to –1.

The position of the PSRJ1622 counterpart candidate shows a systematic offset between the F125W and F160W filters at the same epoch (see Fig. 4). This may be due to a faint, adjacent source, which has affected centroiding (and also possibly the flux measurement). However, the proper motion appears to be consistent between the two filters despite this offset. It is small, nevertheless, so this does not affect our conclusion regarding the origin of PSRJ1622 in SNR G333.9+0.0.

4.3.2. 1RXS J170849-400910

We identify a new candidate counterpart to 1RXS J1708 based on its unusual kinematics. This is neither the first counterpart candidate for 1RXS J1708 nor one of the brighter sources near the south-eastern edge of the X-ray error circle identified by Israel et al. (2003), Durant & van Kerkwijk (2006c). Although the counterpart claimed by Durant & van Kerkwijk (2006c) showed signs of variability (at 3σ significance), Chrimes et al. (2022a) show that this source has an intrinsic H-band absolute magnitude of $\sim$5, far brighter than that of securely identified counterparts (e.g. 4U0142 and SGR0501). The 3.8 kpc distance to this magnetar is based on the optical extinction, which was first estimated from absorption edges in the magnetar X-ray spectra (and is consistent with the A_V–N_H relation Chrimes et al. 2022a), and the distance through the Galactic plane that this extinction implies (Durant & van Kerkwijk 2006c,a). At this distance and with an extinction $A_V = 7.6$, the new counterpart identified in this work has an absolute magnitude of $\sim$8. This is closer to the known population, and coupled with its discrepant kinematics with respect to field, we deem the faint source labelled in Fig. 1 to be the likely counterpart. The IR efficiency of this source is then $\log_{10}(L_{IR}/\dot{E}) = -1.3$, adopting $\dot{E} = 0.58 \times 10^{33}$ erg s^{-1} (Olausen & Kaspi 2014).

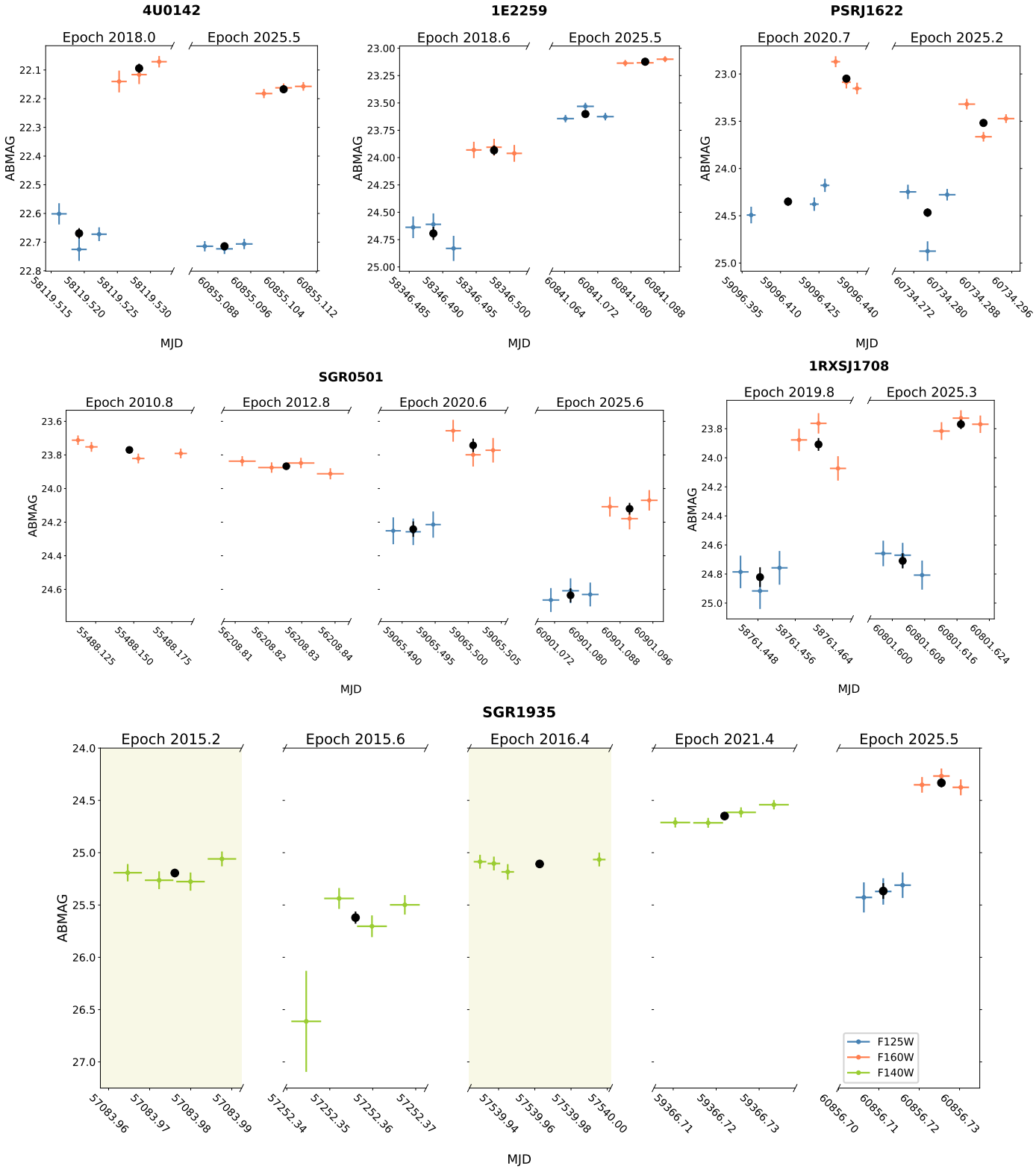


Fig. 3. Near-IR HST _FLT-level light curves for the six counterparts identified in our sample. F125W apparent magnitudes are colour-coded in blue; F160W (which are exclusively fainter than F125W) in orange; and F140W in green (for the first four epochs for SGR1935 only). Note that each subplot has different y-axis limits. The values are reported in the AB system and are not corrected for Galactic extinction. In each epoch, photometry on the combined, drizzled _DRZ image is also shown as a black point with the error bars at the midpoint of the _FLT observations. The 2015.2 and 2016.4 panels for SGR1935 are shaded to indicate that the magnetar was in outburst during these observations (see Sect. 4.5).

4.3.3. CXOUJ164710.2-455216

Finally, we report the likely identification of the infrared counterpart of magnetar CXOUJ1647, which lies outside the Westerlund 1 massive star cluster (Muno et al. 2006). None of the HST sources in the X-ray error circle passes our counterpart selection by the stated criteria. This includes the object identified as a candidate counterpart by Testa et al. (2018), which we refer

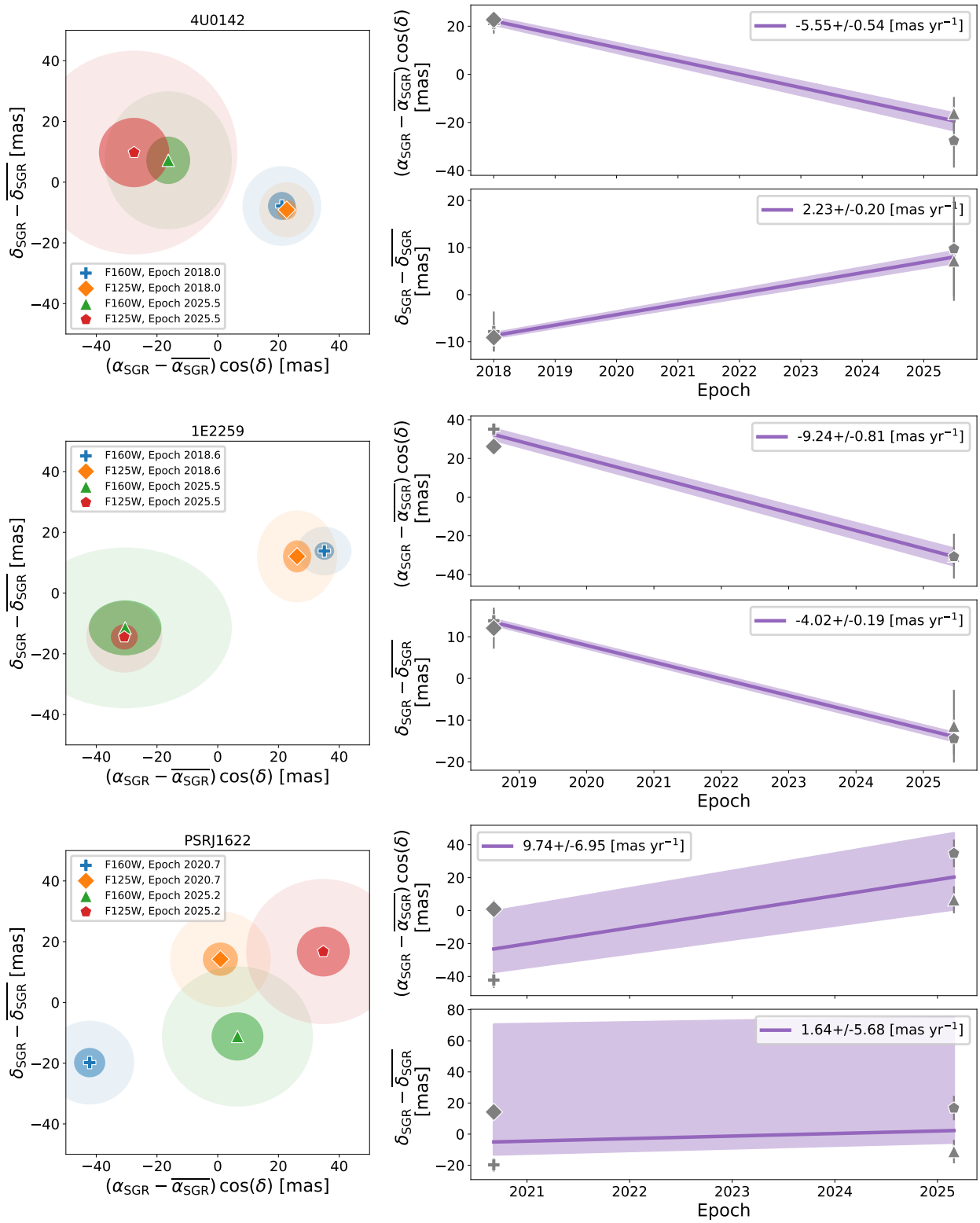


Fig. 4. Proper motion measurements for 4U0142, 1E2259, and PSRJ 1622. Left panels: IR counterpart offsets in α,δ relative to the mean position across the four epochs, with 1σ (dark shading) and 3σ (lighter shading) uncertainties on these offsets. Right panels: Peculiar proper motions determined from each epoch, along with the best fit to all four measurements. The symbols match the epochs and filters shown in the left-hand panel. The proper motion in declination is poorly constrained for PSRJ1622 and could also be expressed as an upper limit on the proper motion of $\mu_\delta < 11.2$ mas yr^{-1} (at the 2σ confidence level). This is continued in Fig. B.5 in the Appendix.

to as source A. However, in the deeper JWST imaging available for the field, a second source (B) is detected close to the centre of the error circle. We find that the extinction-corrected ($A_V = 10$) SED of source B is well described by a power law of the form $f_\nu \propto \nu^{-\alpha}$, with $\alpha = -0.5854 \pm 0.0003$. This is in contrast with $\alpha = 2$ for the Rayleigh-Jeans tail of a black body expected for stellar SEDs. Given the typical power-law SEDs for the magnetars at these wavelengths (Muñoz-Darias et al. 2016;

Hare et al. 2024), the otherwise typically stellar SED of source A, and the unremarkable colours of the other candidates in the X-ray error circle, we deem source B the likely counterpart and label it as such in Fig. 1. The SEDs of sources A and B are shown in Fig. 5, but we leave a full multi-wavelength study of this magnetar to future work (Borghese et al., in prep.). For the purposes of this paper, as source B is only detected in the JWST imaging, no proper motion measurement is possible without a second JWST epoch. This is one of only a few magnetars thus far with a former binary companion candidate (Clark et al. 2014; Sherman et al. 2024), and the proper motion of this former companion candidate is well constrained by *Gaia*, so determining the past trajectory of CXOUJ1647 is an important and viable test of their association.

4.4. Other non-detections

There are eight magnetars in our sample of 14 for which we fail to identify a reliable counterpart candidate in the HST imaging. Of these, SGR1900 and CXOU1647 have candidates, which are detected in previous HST/JWST imaging as discussed above, leaving six with no known counterpart. In these cases, non-detections can occur for two reasons: either the counterpart is undetected in the images, or it is detected but does not exceed our 3σ selection criteria relative to other sources in the field in terms of colour, proper motion, or variability. We list upper limits on the flux, colour, and variability for the six magnetars with no counterpart candidate in Table 1. Similarly, upper limits on the proper motion are provided in Table 2. Note that these proper motion upper limits do not directly reflect the minimum measurable proper motion. Rather, they represent minimum proper motions required for an object to fall outside the 3σ range of the measured proper motions in the image.

Sources in the fields without detections are typically redder than in the fields with identified counterparts, as we can see from the upper limits on the colour for the non-identified sources in Table 1. Along these dustier sight-lines, there are redder sources, so identification through a discrepant colour is less effective. Likewise, upper limits on velocity in the non-detected cases are much higher than the typical values of the known counterparts (see Table 2 and Fig. 6). It is therefore plausible that counterparts to SWIFTJ1822, SWIFTJ1834, SGR1627, CXOUJ1714, SGR1833, and AXJ1818 are detected in the HST imaging but without exhibiting high variability, excessively red colours, or high proper motions. In this scenario we have no way to confidently identify them. On the other hand, higher distances and extinctions, which lead to high upper limits on colour and velocity, also make these counterparts harder to detect. This makes it hard to distinguish between non-detections and non-identifications.

4.5. Light curves and correlation with high energy activity

Near-IR HST light curves for the six counterpart candidates detected in the HST imaging are provided in Fig. 3, including photometry on the individual _FLT level images. These have undergone calibrations including flat fielding and dark subtraction but have not yet been combined with the drizzling process. Some level of variability is apparent in most of these sources, including those that were not selected based on this criteria (e.g. SGR0501). Another example is 4U0142, which displays spectral variability, apparently transitioning from a power law plus blackbody to a pure power law in the optical-IR regime over the course of 20 years (Wang et al. 2006; Hare et al. 2024). However, in the near-IR, the flux only varied at the ∼10–20% level, again demonstrating that IR SEDs (only possible with JWST) reveal much that observations in only 1–2 filters miss.

We searched the literature for reports of flares and outbursts near the epochs of observation shown in Fig. 3. 1RXS J1708 produced a flare on 28 August 2018 (Younes et al. 2020), around two months before the 2018 HST epoch but has otherwise not experienced an outburst in recent years. CXOUJ1714 produced a burst on 5 February 2018, several months before the 2018 HST epoch but has not experienced an outburst since.

SGR1935 has been active in recent years. The first HST epoch for SGR1935 in 2015 occurred during an outburst that began on 22 February 2015, while the 2016 HST imaging was taken shortly after the onset of an outburst on 18 May 2016 (Younes et al. 2017); see also Levan et al. (2018) and Lyman et al. (2022). The 2021 epoch of imaging was taken in between two bursts in February and July of that year (e.g. Borghese et al. 2021; Hamburg et al. 2021); however, we note that the source went into outburst in April 2020 and October 2022 (also associated with FRB emission, Bochenek et al. 2020; CHIME/FRB Collaboration 2020; Tavani et al. 2021; Kirsten et al. 2021; Ibrahim et al. 2024), with frequent bursts in the period in-between. During the final 2025 epoch, the source was in quiescence. We indicate the epochs where the source was active in Fig. 3 (i.e. 2015.2 and 2016.4) by shading the background of the relevant panels. There is no obvious correlation between X-ray activity and NIR flux. For a more detailed analysis of the correlation between SGR1935's X-ray and NIR variability, we refer the reader to Lyman et al. (2022), who also note that the NIR variability does not seem to track activity at high energies.

Finally, CXOUJ1647 was active from May 2017 through to at least April 2018, producing multiple bursts in this time (Borghese et al. 2019), but as discussed above, the likely NIR counterpart was not detected in any of the HST epochs. Analysis of the X-ray light curve of this source from 2023 onwards in ongoing. No bursts, outbursts, or flares were found near any of the epochs for the other magnetars in the sample.

4.6. Transverse velocities

For the six NIR counterpart identifications with proper motion measurements, the fits are provided in Figs. 4 and B.5. In each of the four cases where we measure the proper motion of an object – already previously measured – our results are fully consistent with the previous results (listed in Table 2), with uncertainties typically reduced by a factor of ∼2. We converted the peculiar proper motions into transverse velocities by adopting the distances listed in Table 2. Our six magnetar velocities are supplemented by XTE J1810 (Ding et al. 2020), 1E1547 (Deller et al. 2012), SGR1806, SGR1900 (Tendulkar et al. 2012), and SWIFTJ1818 (Ding et al. 2024), yielding a total of eleven magnetars with transverse velocity measurements. The proper motions, distances, and velocities of these additional six magnetars are provided in Table 2. The transverse velocity of SGRJ1745 has also been measured (Bower et al. 2015), but it is likely bound to Sgr A*, so we do not consider it further.

The cumulative distribution of the eleven magnetar velocities is shown in Fig. 6. We generated 1000 realisations of the distribution by sampling the proper motion uncertainties, assuming they are Gaussian distributions. We note that distance uncertainties are not accounted for, and although these can be considerable (only two magnetars have a parallax measurement, Ding et al.

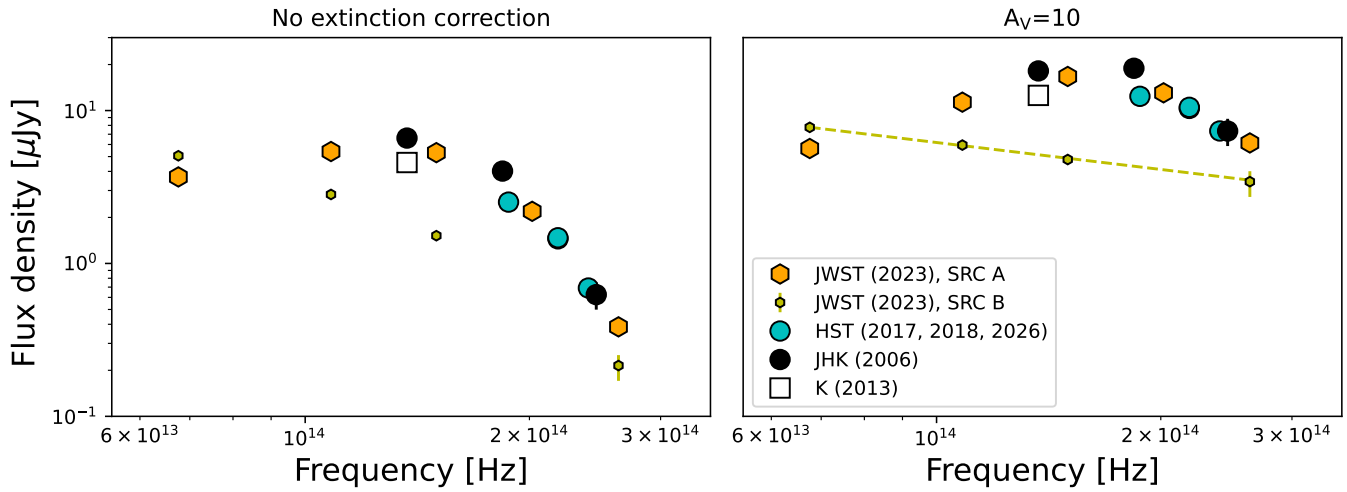


Fig. 5. NIR SED of the two objects near the centre of the X-ray localisation of CXOUJ1647. One is a source previously identified as a counterpart candidate (Testa et al. 2008). The other has a power-law SED after extinction correction, similar to other known magnetar counterparts; therefore, we consider it the likely counterpart. Measurements of the brighter, previously identified source were derived from Testa et al. (2018, for the 2006 JHK_s and 2013 K_s points), this work, Chrimes et al. (2022b, HST), and Guarcello et al. (2025, for the JWST/NIRcam data). Note that in Fig. B.4, neither of the objects in the X-ray error circle with a proper motion measurement represents the power-law source, since it is undetected in the HST images.

Table 1. Photometry of the NIR counterparts reported in this work (uncorrected for Galactic extinction).

Magnetar	Epoch	Filter	m(AB)	Flux [μJy]	F125W-F160W	|Δmag|
4U0142	2025.5	F125W	22.71 ± 0.01	2.99 ± 0.03	0.54 ± 0.01	0.04 ± 0.02
	2025.5	F160W	22.17 ± 0.01	4.92 ± 0.05		0.07 ± 0.02
SGR0501	2025.6	F125W	24.64 ± 0.04	0.51 ± 0.02	0.52 ± 0.06	0.39 ± 0.06
	2025.6	F160W	24.12 ± 0.04	0.82 ± 0.03		0.38 ± 0.05
PSRJ1622	2025.2	F125W	24.47 ± 0.05	0.59 ± 0.03	0.75 ± 0.06	0.10 ± 0.06
	2025.2	F160W	23.52 ± 0.03	1.42 ± 0.04		0.47 ± 0.05
SGR1935	2025.5	F125W	25.37 ± 0.08	0.26 ± 0.02	1.04 ± 0.09	
	2025.5	F160W	24.33 ± 0.04	0.67 ± 0.02		
1E2259	2025.4	F125W	23.60 ± 0.02	1.32 ± 0.02	0.48 ± 0.03	1.09 ± 0.06
	2025.4	F160W	23.12 ± 0.02	2.05 ± 0.04		0.81 ± 0.05
1RXSJ 1708	2025.3	F125W	24.71 ± 0.05	0.47 ± 0.02	0.94 ± 0.06	0.11 ± 0.09
	2025.3	F160W	23.77 ± 0.03	1.13 ± 0.03		0.14 ± 0.06
CXOUJ1647	2023.2	F115W	25.57 ± 0.20	0.21 ± 0.04		
	2023.2	F200W	23.45 ± 0.04	1.51 ± 0.05		
	2023.2	F277W	22.77 ± 0.02	2.83 ± 0.05		
	2023.2	F444W	22.14 ± 0.01	5.06 ± 0.05		
SWIFTJ1822	2025.2	F125W	<25.6	<0.21	<1.30	<0.27
	2025.2	F160W	<25.4	<0.24		<0.26
SWIFTJ1834	2025.2	F125W	<26.7	<0.07	<3.31	<0.22
	2025.2	F160W	<26.3	<0.11		<0.23
SGR1627	2025.3	F125W	<26.4	<0.10	<2.40	<0.26
	2025.3	F160W	<25.9	<0.16		<0.24
CXOUJ1714	2025.3	F125W	<25.2	<0.31	<1.70	<0.26
	2025.3	F160W	<24.4	<0.65		<0.25
SGR1833	2025.5	F125W	<26.4	<0.10	<3.49	<0.26
	2025.5	F160W	<25.9	<0.16		<0.26
AXJ1818	2025.4	F125W	<26.4	<0.10	<1.88	<0.29
	2025.4	F160W	<25.9	<0.16		<0.27

Notes. For details of the observations and previous HST epochs in these filters, see Table A.1 and Fig. 3. For SGR0501 we use the 2020.6 epoch for the F160W Δmag. The counterpart of CXOUJ1647 is undetected in the HST imaging, and we instead list here the JWST/NIRcam photometry from Guarcello et al. (2025). Below the horizontal line, we list the 3σ limiting magnitudes and fluxes for the six objects in this sample for which no reliable counterpart candidate is known (i.e. the eight shown in Figs. B.3 and B.4, excluding CXOUJ1647, which was detected with JWST, and SGR1900; see Sect. 4.2.2). We also list 3σ upper limits on the F125W-F160W colour and Δmag, which a source would need to exceed to be selected as a candidate according to the criteria outlined in Sect. 3.3. In these cases, we are unable to say whether a counterpart is undetected or detected but not selected.

2020, 2024), they are hard to formally quantify. Each step in the distribution is labelled by the method through which the best available proper motion was measured. We note that parallaxes are unlikely to strongly influence our proper motion measurements. For even the closest magnetars (~1 kpc), the maximum positional shift due to parallax is ~1 mas – hence <0.2 mas yr^{-1} over the baselines probed – if such a shift were misattributed to proper motion. This is typically a factor of ~10 or more lower than the measured proper motions (see Table 2).

4.7. Birth sites

For the six counterparts with proper motions identified in Sect. 4, we produced 100 realisations of their past trajectories by sampling from the proper motion uncertainties and plotting these vectors with lengths corresponding to (i) their characteristic age (from the McGill catalogue, Olausen & Kaspi 2014, and references therein) and (ii) an age ten times older to account for the possibility of inaccurate characteristic ages. We note that characteristic ages are typically upper limits but that they could be higher if $\dot{P}$ was measured outside quiescence when spin-down rates vary significantly (e.g. Woods et al. 2002; Kaspi & Gavriil 2003; Mori et al. 2013). Since the influence of the Galactic potential is not expected to significantly affect the trajectory of natal neutron stars on timescales of less than ~10 Myr (Disberg et al. 2024), the linear propagation of past trajectories is expected to be reliable for our purposes. The results are shown in Fig. 7.

SGR1935 can be traced within a factor of a few of its characteristic age back to the geometric centre of SNR G57.2+08, as first demonstrated by Lyman et al. (2022). 1E2259 also has a past trajectory, which passes close to the centre of a SNR (CTB 109, Fahlman & Gregory 1981; Tendulkar et al. 2013). However, the magnetar must be significantly younger than its characteristic age, as this would otherwise place the birth site well outside the SNR. As first shown by Chrimes et al. (2025), the direction and magnitude of SGR0501's proper motion rules out an origin in the nearby SNR HB9, and no other plausible birth site has yet been identified. Similarly, no candidate SNR or stellar cluster has been found along the past trajectory of 4U0142 (see also Tendulkar et al. 2013). SNR G127.1+0.5 lies within 2 deg of 4U0142 but in the opposite direction. The past trajectory of PSRJ1622 is consistent, within a factor of ~2 of its characteristic age, with the centre of SNR G333.9+0.0 (first noted as a possible origin of this magnetar by Anderson et al. 2012).

Finally, the past trajectory of the object we claim to be the counterpart of 1RXS J1708 intersects SNR G346.6-0.2. There is no other neutron star association with this SNR (Green 2025). 1RXS J1708 would have to be ~10 times its characteristic age for this association to hold, although such a large kinematic age is not unprecedented. XTEJ1810 would have to be ~70 kyr old to be associated with SNR G11.0-0.0 (Helfand et al. 2007; Ding et al. 2020), and similar discrepancies have been seen in pulsars (e.g. Espinoza et al. 2022). Despite the past spatial coincidences, the reliability of these associations is called into question by the large discrepancies between the SNR and kinematic ages. Furthermore, distance estimates for SNR G346.6-0.2 are in the ~5.5–11 kpc range (Koralesky et al. 1998; Sano et al. 2021), higher than the estimate of 3.8 ± 0.5 claimed for 1RXS J1708 based on red clump stars along that sight-line (Durant & van Kerkwijk 2006a). The F160W (approximate H-band) absolute magnitude of the counterpart assuming 3.8 kpc and A_V = 7.6 would be ~5, similar to known counterparts (Chrimes et al. 2022a). Placing it at greater distances (up to the other extreme of 11 kpc) and behind higher extinction (up to the total Galactic extinction along this sight-line of A_V ~ 60; Schlafly & Finkbeiner 2011) would imply that the source is intrinsically luminous and blue, inconsistent with known magnetar counterparts. It could feasibly then be a massive star but, given its co-location with the X-ray source, would presumably have to be a non-interacting companion to the magnetar, where the binary has been given a large natal kick without being unbound. The SNR has an estimated age of ~12–14 kyr (assuming d = 8–9 kpc), and this would only decrease if placed at a shorter distance (Auchettl et al. 2017; Sano et al. 2021). We proceed under the assumption that the SNR is at the lower end of the distance estimates and that 1RXS J1708 was born in this supernova. We nontheless acknowledge the significant uncertainties in this interpretation.

5. Discussion

5.1. Magnetar natal kicks

The magnetar and young pulsar velocity distributions shown in Fig. 6 appear similar, with a possible dearth of magnetars at the high velocity end. We carried out Anderson-Darling tests between 1000 realisations of the magnetar distribution, sampling from their proper motion uncertainties, and the transverse velocity distribution of young pulsars (Disberg & Mandel 2025). We only considered magnetars with a measured proper motion, since the upper limits (corresponding to non-detections or non-identifications) may instead be cases where the counterpart was below the detection threshold of the image. To avoid negative v_t values, we performed log-normal sampling of the velocities. P-values >0.05 are found in only 3% of the realisations. This formally rejects the null hypothesis that the magnetar velocities are drawn from the same underlying distribution as pulsars. The 16th, 50th, and 84th percentiles of the magnetar velocity distributions yield $v_t = 154^{+141}_{-86}$ km s^{-1}. We repeated the process, each time removing the fastest 1% of the young pulsar distribution. We reached 5% of realisations with $p > 0.05$ once the fastest ~15% of pulsars were removed. Similar to Ding et al. (2024), we therefore conclude that there is tentative evidence for a difference between the distributions, although this tension could plausibly be reduced by revisions to magnetar distance. For example, we find that any distance revisions resulting in just two magnetars in the sample exceeding a velocity of >500 km s^{-1} would render the samples statistically indistinguishable.

Given our selection criteria, slow-moving magnetars, which are neither particularly red or variable nor have similar magnitudes in the relevant epochs, may have been missed. Our selection may therefore be biased towards faster moving objects. For example, the source in the error circle of SWIFTJ1834 appears to be moving against the bulk motion of objects in the field (Fig. B.3). However, its displacement across the 5-year baseline is only ~2σ outside the scatter of all sources in the field. Given that the source is also not anomalous in colour and variability, we cannot yet confidently claim it as the counterpart. Further imaging on longer temporal baselines could determine whether this source truly has a discrepant proper motion for its field. However, even in the cases where we only have an upper limit on the velocity (assuming the counterpart was detected at all), the magnetars would need to be close to these upper limits to extend the magnetar distribution into the pulsar high velocity tail, as shown in Fig. 6.

Conversely, for high proper motions >15 mas yr^{-1} over baselines of >5 years, the object could have moved sufficiently such

Table 2. Proper motion, distance, and transverse velocity information for the sample of eleven magnetars with these measurements, as defined in Sect. 4.6.

Magnetar	$\mu_\alpha \cos(\delta)$ [mas yr^{-1}]	μ_δ [mas yr^{-1}]	d [kpc]	Distance Ref.	v_t [km/s]	$v_{t,d}$ [km/s]
PSRJ1622	9.7 ± 7.1	1.6 ± 5.8	~5	Yao et al. (2017)⋆	260 ± 180	260^{+198}_{-192}
1E2259	-9.2 ± 0.8	-4.0 ± 0.2	3.2 ± 0.2	Kothes & Foster (2012)	153 ± 11	153 ± 14
4U0142	-5.5 ± 0.5	2.2 ± 0.2	3.6 ± 0.4	Durant & van Kerkwijk (2006a)	102 ± 9	102 ± 15
SGR0501	4.4 ± 0.4	-4.0 ± 0.5	2 ± 1	Lin et al. (2011)	57 ± 4	57 ± 31
SGR1935	-0.3 ± 0.4	2.3 ± 0.7	6.6 ± 0.7†	Zhou et al. (2020)	72 ± 20	72 ± 21
1RXSJ 1708	-13 ± 2	2.0 ± 1.5	3.8 ± 0.5	Durant & van Kerkwijk (2006a)	240 ± 40	240 ± 50
Magnetar	$\mu_{\alpha,\mathrm{prev}} \cos(\delta)$ [mas yr^{-1}]	$\mu_{\delta,\mathrm{prev}}$ [mas yr^{-1}]		μ_{prev} Ref.		
1E2259	-9.9 ± 1.1	-3.0 ± 1.1		Tendulkar et al. (2013)		
4U0142	-5.6 ± 1.3	2.9 ± 1.3		Tendulkar et al. (2013)		
SGR0501	4.1 ± 0.7	-3.5 ± 0.4		Chrimes et al. (2025)		
SGR1935	-0.7 ± 0.8	3.1 ± 1.6		Lyman et al. (2022)†		
Magnetar	$\mu_\alpha \cos(\delta)$ [mas yr^{-1}]	μ_δ [mas yr^{-1}]	d [kpc]	Distance Ref.	v_t [km/s]	
SWIFTJ1822	<5.7	<7.5	1.6 ± 0.3	Scholz et al. (2012)	<71	
SWIFTJ1834	<6.1	<7.5	4.2 ± 0.3	Leahy & Tian (2008)	<193	
SGR1627	<5.8	<5.9	11.0 ± 0.3	Corbel et al. (1999)	<432	
CXOUJ1714	<5.5	<6.0	9.8 ± 1.5	Blumer et al. (2019)	<380	
SGR1833	<5.1	<6.9	<10⋆⋆		<408	
AXJ1818	<6.4	<8.9	<10⋆⋆		<521	
Magnetar	$\mu_{\alpha,\mathrm{prev}} \cos(\delta)$ [mas yr^{-1}]	$\mu_{\delta,\mathrm{prev}}$ [mas yr^{-1}]	d [kpc]	μ_{prev}, d and $v_{t,d}$ Ref.		$v_{t,d}$ [km/s]
1E1547	4.8 ± 0.5	-7.9 ± 0.3	6 ± 2	Deller et al. (2012)		280^{+130}_{-120}
SGR1806	4.2 ± 0.9	7.0 ± 1.8	9 ± 2	Tendulkar et al. (2012)		350 ± 100
SGR1900	2.7 ± 0.2	4.8 ± 0.4	12.5 ± 1.6	Tendulkar et al. (2012)		130 ± 30
XTE J1810	$-3.79^{+0.05}_{-0.03}$	-16.2 ± 0.1	$2.5^{+0.4}_{-0.3}$	Ding et al. (2020)		198^{+29}_{-23}
SWIFTJ1818	-3.57 ± 0.02	-7.72 ± 0.06	$9.4^{+2.0}_{-1.4}$	Ding et al. (2024)		48^{+50}_{-16}

Notes. The table is split into four sections. Top section: Peculiar proper motions for the six NIR counterparts (re-)identified in this work. The proper motions of PSRJ1622 and 1RXS J1708 are newly reported. Uncertainties on the v_t velocities do not include uncertainties on the distance, while the final column lists the $v_{t,d}$ velocities, which also include the quoted distance uncertainties (a 20% distance uncertainty is adopted for PSRJ 1622). Second section: Previous measurements for the four previously known counterparts re-identified in this work. Third section: 3σ upper limits on proper motion and velocity for the six cases where no counterpart is identified, assuming that the counterpart was detected in the image but not discrepant in colour, variability, or proper motion. Final section: Previously reported proper motion measurements, distance estimates, and transverse velocities for five additional magnetars, whose measurements are reported in the literature. Velocity uncertainties include the quoted distance uncertainty in each case. For the case marked with a single star (⋆), see also Sect. 4.3.1. For the case marked with a dagger (†), see also Bailes et al. (2021). For the cases marked with two stars (⋆⋆), i.e. when no distances are available, we assume $d < 10$ kpc.

that it is now unrecognizable as the same object. A standard matching radius of 75 mas was used to identify the common sources between images but is extended by a factor of 2–3 inside the X-ray error circles to account for the possibility of the high proper motion objects here. However, very high proper motion objects could have moved outside the X-ray error circle entirely, as the error circles are static and are typically derived from observations taken several years prior to the first HST observations (Olausen & Kaspi 2014). This is a potential bias against the detection of very high velocity objects. To investigate, we visually inspected the images of every magnetar, blinking the images between epochs to check for high proper motions and/or objects leaving the X-ray error circle. This is effective because large changes in position are obvious by eye (e.g. the motion of 1RXSJ 1708, with $\mu \sim 13$ mas yr^{-1}, is clearly visible when the images are blinked). We find no high-proper motion objects in the vicinity of the magnetar X-ray localisations, aside from those already identified as counterparts with the default selection criteria. We therefore conclude that a potential selection bias against very high v_t objects has not played a role in this sample.

Finally, we investigated whether there were any correlation between magnetar magnetic fields and their transverse velocities, which might provide insight into their formation channels. Eleven magnetars have transverse velocity (Table 2) and magnetic field strength measurements (Olausen & Kaspi 2014). Notwithstanding the large velocity uncertainties, a Spearman rank correlation test yields a p-value of 0.36, indicating no evidence for a correlation between these two parameters.

5.2. Kinematic versus characteristic ages

For the sample of eleven magnetars with proper motion measurements, we collate information about their characteristic ($P/\dot{P}$ spin-down) age τ_c in Table 3. Spin-down ages assume a braking index $n = 3$ (e.g. Hamil et al. 2015), a dipolar and constant magnetic field, and $P_{\mathrm{init}} \ll P$. These assumptions may not hold, particularly for magnetars, where the excess luminosity above that expected from spin-down is attributed to the decay of the magnetic field (Thompson & Duncan 1995). Therefore, τ_c may be an unreliable age indicator and is an upper limit, unless there are

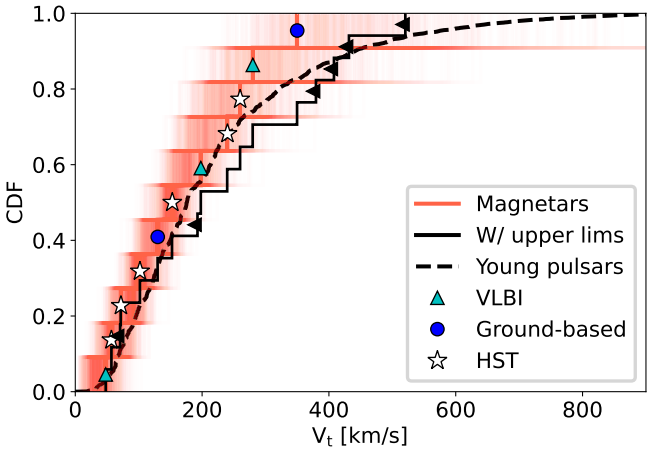


Fig. 6. Peculiar transverse velocity distribution (red) of all magnetars with a velocity measurement (i.e. transverse velocities after correcting for an assumed distance and hence LSR). Each step in the distribution is labelled according to the method used to obtain the best available proper motion. One thousand random samples of the velocities, within their uncertainties (including distance uncertainty; see Table 2), are also shown. The solid black line represents the magnetar distribution with the six upper limits listed in Table 2. The steps corresponding to these upper limits are marked with left-facing triangles. The transverse velocity distribution of the pulsars with age <10 Myr (the fiducial distribution of Disberg & Mandel 2025) is shown with a dashed black line.

P-$\dot{P}$ variations due to variability during outbursts (Kaspi & Gavriil 2003; Mori et al. 2013).

We also list in Table 3 the angular offset to any SNR or stellar cluster association, where available, and report a kinematic age τ_k. The kinematic age uncertainties are propagated solely from the uncertainty on the proper motion, while the uncertainty on the point of origin within the SNR or cluster is not quantified. Kinematic ages offers an independent constraint. They are defined as the time it would have taken, given the observed proper motion, to have travelled from the (estimated centroid of the) birth site to the current position. We further list the ages of associated SNRs in Table 3, where available.

In the left-hand panel of Fig. 8, we plot τ_c versus τ_k for each case where a birth site has been identified. In every case the discrepancy is in the direction of the spin-down age underestimating the true age, with the sole exception of 1E2259. The mean shift (excluding 1E2259) is a factor of 4 ± 1 increase over the characteristic age. In general, characteristic ages are not reliable because magnetar spin-down rates are known to vary. Moroever, the magnetic field is not constant and is known not to be a simple dipole (e.g. Esposito et al. 2009). However, these effects are typically expected to act in the direction of decreasing the true age with respect to the characteristic age, so the result shown in Fig. 8 is surprising, with the exception of 1E2259, which stands out as the only example following the expected behaviour.

Figure 8 demonstrates the value of kinematic ages as an independent way to determine magnetar and SNR ages simultaneously, ultimately constraining the physics governing the spin-down evolution of magnetars (e.g. Tendulkar et al. 2012; Li et al. 2026). However, the kinematic ages are more uncertain than listed in Table 3 and shown in Fig. 8, where the uncertainties are propagated solely from the proper motion uncertainties. In addition, there are the uncertainties regarding (i) the magnetar's origin within in the SNR or cluster, which might not necessarily be the assumed geometric centre, and (ii) the reliability of the birth site association, as our assigned birth site may be incorrect. In at least two cases (1RXSJ1708 and XTE J1810), there is a large discrepancy between the SNR age and kinematic age, which is challenging to explain and calls these associations into question. Furthermore, SGR1900 and SGR1806 have cluster associations, and there is a known bias against SNR detections in clusters (see the next subsection). Therefore, the true birth site may be closer than the cluster centroids assumed for the kinematic ages. If we assume that these four objects have spurious kinematic ages and remove them from Fig. 8, the mean shift reduces to a factor of 3 ± 1, and the significance of the result is further reduced when the uncertainty in the point of origin within the SNR is considered (e.g. SGR1935 need not have originated at the geometric centre of SNR G57.2+08). On the other hand, if the SNRs associated with magnetar formation have already faded, given the distribution of SNR ages (Fig. 8), this might also suggest a true age, which is greater than the characteristic age. To quantify these uncertainties, a detailed study of the observational biases at different wavelengths, the chance alignment probability, and the evolution of SNRs throughout the Galactic plane would be needed.

If the result suggested by Fig. 8 holds, it would imply fewer young neutron stars in the Galaxy than suggested by their characteristic ages, thereby affecting their birth rates and the fraction of neutron stars born as magnetars (Beniamini et al. 2019; Jawor & Tauris 2022; Sautron et al. 2025; Pardo-Araujo et al. 2026). For example, in this sample, increasing the characteristic ages by a factor of three reduces the number of magnetars younger than 2 kyr by a factor of two and those younger than 20 kyr by a factor of 1.3. This would imply a corresponding reduction in the fraction of neutron stars born as magnetars, a reduction in the completeness of the Galactic magnetar sample, or some combination thereof. However, we stress again that these conclusions depend entirely on both the counterpart and birth site associations being robust.

5.3. Magnetars without SNR or cluster associations

A parent SNR or stellar cluster is identified in every case. We ask whether this is surprising, given the age of the magnetar and assuming that the characteristic age is representative (within some scatter, as described above). In the right hand panel of Fig. 8, we plot the cumulative distribution of τ_c for the eleven magnetars with a proper motion, which hence provides an opportunity to determine the birth site. Each step in the distribution is labelled by the magnetar name and whether a SNR association is established. Also shown is the age distribution of the Galactic SNRs (Ranasinghe & Leahy 2023). All 11 magnetars lie in the same age range as the Galactic SNRs, and seven have at least a tentatively associated SNR, which is consistent with its past trajectory. Although excluded here due to the likely influence of Sgr A* on its motion, SGR1745 has also been linked with a SNR (Ponti et al. 2015; Yalinewich et al. 2017).

Two other magnetars, SGR1900 and SGR1806, are not associated with a SNR. Both have ages at the lower end of the Galactic SNR age distribution. However, they are linked with massive stellar clusters (Tendulkar et al. 2012). This may reflect different formation channels. For example, one channel could involve ejected progenitors that travel far from their birth clusters before undergoing a supernova (e.g. Eldridge et al. 2011), while the other could involve a progenitor that remains in situ but produces weak SNe. However, there are known biases against SNR detection in clusters due to to the merging of individual remnants in dense environments (e.g. Vasiliev et al. 2017), confusion with the diffuse background and HII region emission (Anderson et al.

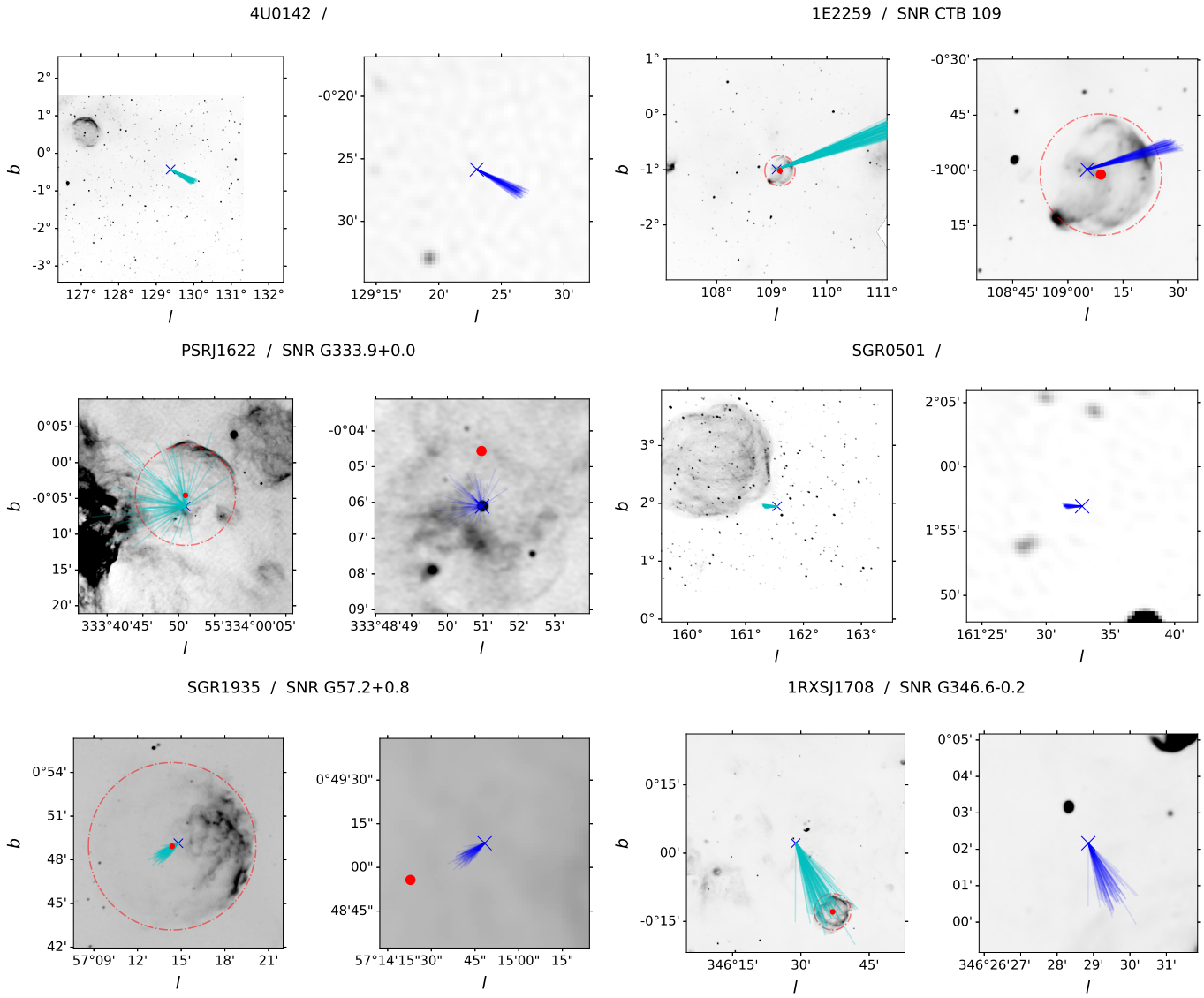


Fig. 7. Past trajectories of the magnetars for which we measured a new or improved proper motion in this work. In each case we randomly sampled 100 ($\mu_\alpha \cos(\delta)$, μ_δ) pairs from the measured proper motions and their uncertainties, assuming Gaussian distributions. The lengths of the past trajectory vectors correspond to (i) ten times the characteristic age (cyan) and (ii) the characteristic age (blue). The radial extent of SNRs, which are plausibly associated with a magnetar, are indicated with the dashed red lines, and their approximate centres are marked with a red dot. The background radio images are from the 1.4 GHz Canadian Galactic Plane Survey (4U0412, 1E2259 and SGR0501, Taylor et al. 2003) and the MeerKAT 1.3 GHz Galactic Plane Survey (PSRJ1622, SGR1935 and 1RXSJ 1708, Goedhart et al. 2024). No suitable SNR birth site can be identified for 4U0412 and SGR0501. Analogous searches for stellar clusters in optical imaging have also produced null results for these objects (Tendulkar et al. 2013; Chrimes et al. 2025).

2017, 2025; Green 2019), and the small angular sizes of young SNRs in dense environments (Verberne & Vink 2021).

Finally, SGR0501 and 4U0142 are the only two magnetars with a well-constrained past trajectory but no obvious SNR or parent stellar cluster. They are among the oldest objects in the sample, so plausibly an associated SNR may have already faded, although SNRs with similar ages are known. If the SNR HB9 were the origin of SGR0501 (neglecting for a moment the direction of the proper motion vector), the kinematic age would be $\sim 10^6$ years, in the extreme tail of the SNR age distribution. Given the spin-down age of ~15 kyr, this would be by far the largest discrepancy in the left panel of Fig. 8. Although we show characteristic ages in the right panel of Fig. 8, the true (kinematic) age of 1E2259 is a factor of ~10 younger, so the detection of the associated SNR is consistent known SNR ages, in contrast with the 4U0142 and SGR0501 non-detections. If the association of 1RXSJ 1708 with SNR G346.6-0.2 holds, it must be a factor of ~10 older than the characteristic age, which would also make SNR G346.6-0.2 one of the oldest SNRs known.

Crucially, in the other cases where no SNR was identified (SGR1900 and SGR1806), massive star clusters were nevertheless present. Given that the lifetimes of even massive stars are at least two orders of magnitude longer than the characteristic ages of SGR0501 and 4U0142 and their positions in the Galactic anti-centre direction with relatively low extinction on their sight-lines, the lack of massive stars or clusters along their past trajectories is also surprising. Non-core-collapse channels, such as accretion-induced collapse (Nomoto & Kondo 1991) and low-mass neutron star mergers (Giacomazzo & Perna 2013; Piro et al. 2017), are plausible alternative progenitor channels

Table 3. Characteristic ages τ_c (from the McGill catalogue and references therein Olausen & Kaspi 2014), birth sites, and the approximate angular offsets to (the centres of) the proposed birth sites.

Magnetar	τ_c [kyr]	Birth site	Birth site Ref(s).	Ang. sep. [arcmin]	τ_k [kyr]	τ_{SN} [kyr]	τ_{SN} Ref.
PSRJ1622	4	SNR G333.9+0.0	Anderson et al. (2012)	1.5	8 ± 6	<6	Levin et al. (2010)
1E2259	230	SNR CTB 109	(Tendulkar et al. 2013)	3	24 ± 2	12.7 ± 0.8	Leahy et al. (2020)
4U0142	68	?	(Tendulkar et al. 2013)	–	–	–	–
SGR0501	15	?	(Chrimes et al. 2025)	–	–	–	–
SGR1935	3.6	SNR G57.2+0.8	Lyman et al. (2022)	0.6	16 ± 4	$\gtrsim 16$	Zhou et al. (2020)
1RXSJ 1708 †	9	SNR G346.6-0.2	This work	20	90 ± 15	14 ± 2	Sano et al. (2021)
1E1547	0.69	SNR G327.24-0.13	Camilo et al. (2007)	0.5	3 ± 1	–	–
SGR1806	0.24	Stellar cluster	Tendulkar et al. (2012)	0.07	0.65 ± 0.19	–	–
SGR1900	0.9	Stellar cluster	Tendulkar et al. (2012)	0.33	6 ± 1	–	–
XTE J1810 †	11	SNR G11.0-0.0	(Helfand et al. 2007)	19	70^{+8}_{-10}	$\lesssim 3$	Ding et al. (2020)
SWIFTJ1818	0.24	SNR	Ibrahim et al. (2023)	0.2★	$1.20^{+0.40}_{-1.15}$	–	–

Notes. The six above the horizontal line have an HST-derived proper motion; no birth site has been found for SGR0501 and 4U0142. The kinematic ages τ_k are listed for the remaining five magnetars with a proper motion constraint and candidate birth site (see Sect. 4.6 and Fig. 6). All values are approximate, as we can neither determine the precise place of origin in a cluster nor the exact centre of a SNR remnant (due to non-symmetric expansion). The last columns list SNR ages τ_{SN}, based on size and where available, along witih their references. Those marked with a star (★) were judged by eye from Fig. 7 of Ibrahim et al. (2023). Magnetar-SNR associations marked with a dagger (†) should be treated with caution due to the large discrepancy between the characteristic and kinematic ages, and the SNR age.

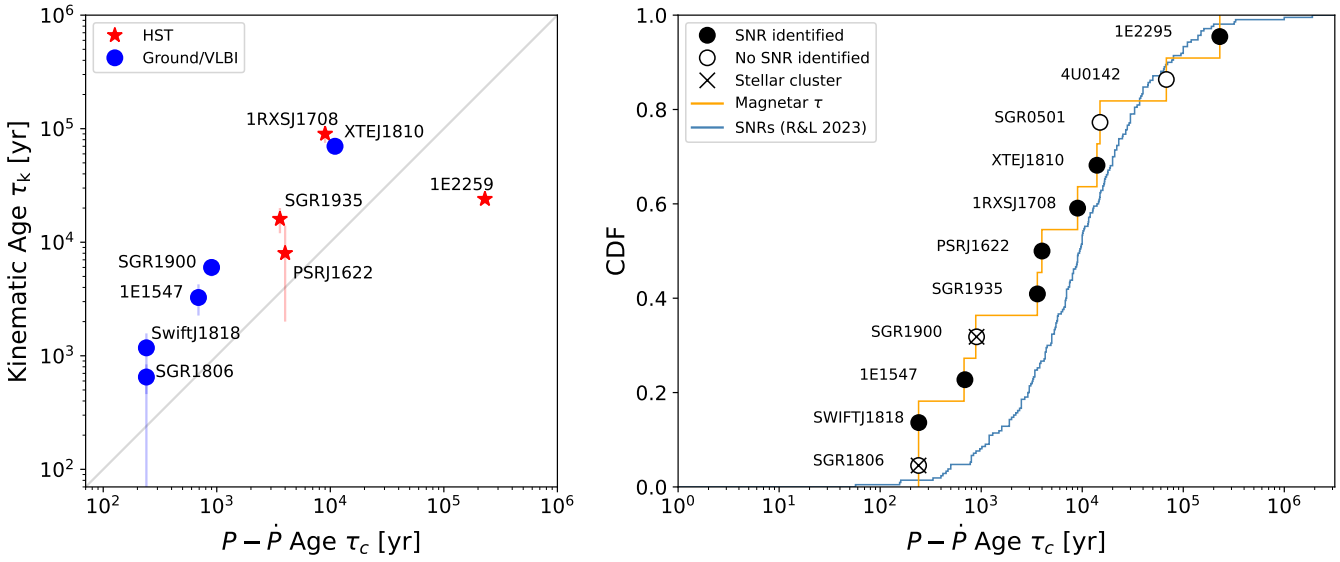


Fig. 8. Left panel: Kinematic vs characteristic (spin-down) ages for the subset of nine magnetars with (i) a proper motion measurement and (ii) a SNR or stellar cluster along their past trajectory (see Table 3). The diagonal grey line represents $\tau_c = \tau_k$. The characteristic ages (τ_c) are upper limits. The kinematic ages (τ_k) assume an origin in the approximate centre of the associated SNR or cluster, and their uncertainties are propagated solely from the uncertainty on the proper motion. The SNR associations for XTEJ1810 and 1RXSJ1708 should be treated with caution due to the large discrepancy between the characteristic, SNR and kinematic ages. Right panel: Cumulative distribution function of the characteristic ages for the eleven magnetars with a proper motion measurement (not including the Galactic centre object SGR1745). Each object is labelled according to whether it has a SNR/stellar cluster association, or no candidate birth site. Also shown is the cumulative distribution of the Galactic SNR ages (Ranasinghe & Leahy 2023).

(Chrimes et al. 2025). However, these interpretations are challenged by the low Galactic latitudes of SGR0501 and 4U0412, which should not necessarily be favoured by pathways involving white dwarfs (unconfined to the disc) or neutron star mergers (potentially kicked out of the plane). Similarly, the explanation that their progenitor stars were ejected from their parent clusters – either by the supernova of a companion (e.g. Blaauw 1961; Renzo et al. 2019) or via dynamical interactions (e.g. Poveda et al. 1967; de Wit et al. 2005) – faces a similar issue. In such a scenario, massive runaway stars could travel hundreds or even thousands of parsecs (easily enough to escape the Galactic plane) before undergoing a supernova (e.g. Eldridge et al. 2011).

Finally, we ask whether the cluster-associated, SNR-associated, and non-associated magnetars have distinct properties. In terms of velocities, the cluster-associated magnetars occupy the middle of the transverse velocity distribution, while 4U0142 and SGR0501 lie at the lower end. Although the sample size is small, we note that the two cluster-associated

magnetars (SGR1806 and SGR1900) also have the strongest magnetic fields in the sample and are among the youngest, while 4U0142 and SGR0501 are among the oldest. This may be consistent with a scenario in which young SNRs in clusters are hard to detect, and older remnants have faded, as discussed above.

6. Conclusions

In this paper, we searched for NIR counterparts to Galactic magnetars in repeat HST (and in one case single-epoch JWST) imaging. We re-discovered the counterparts of four magnetars (4U0142, 1E2259, SGR0501, and SGR1935), reducing the uncertainties on their proper motions, and report new candidates for a further three (PSRJ1622, 1RXSJ 1708, and CXOUJ1647), measuring the first proper motions for PSRJ 1622 and 1RXSJ 1708. We find that magnetar characteristic ages may underestimate their true ages, based on SNR and stellar cluster associations. However, this results hinges on the reliability of these birth site associations.

We show that magnetar transverse velocities and birth sites are broadly similar to that of young pulsars, with the notable exceptions of SGR0501 and 4U0142 for which no candidate birth sites have yet been identified. This is consistent with the idea that magnetars evolve into other classes of neutron stars, such as X-ray dim isolated neutron stars (e.g. Borghese & Esposito 2023; Gençali & Ertan 2024), and with searches for companion stars (Chrimes et al. 2022a), both of which broadly match expectations for neutron stars in general. However, there is some evidence (Sherman et al. 2024) that magnetars may primarily form in the core collapse of merger products based on a lack of unbound companions (see also Tendulkar et al. 2012; Schneider et al. 2019, 2020; Shenar et al. 2023). We also find tentative evidence for a dearth of high-velocity magnetars compared to young pulsars. If real, this effect may arise from an as yet unidentified physical preference in the progenitor population producing magnetars and/or a difference in their post-formation velocity evolution.

The faintness of the new counterparts identified in this work (>23.5 AB at 1.6 µm), coupled with crowded sight-lines through the Galactic plane, demonstrates the strength of sensitive, high spatial resolution NIR observations for multi-wavelength neutron star studies. We also showed that, while effective, magnetar counterpart selection based on colour, variability, and proper motion may miss some objects and could be biased towards higher transverse velocities. For example, the discovery of the counterpart of CXOUJ1647 required a JWST SED. Future multi-filter and multi-epoch JWST studies will enable redder, fainter, and higher spatial resolution observations. The constraints achievable depend on the signal-to-noise (S/N) ratio of the source, but for targets detected with S/N = 20, we estimate that with observing baselines of three years, NIRcam observations can probe proper motions as small as 1 mas yr^{-1}. At this level, parallaxes may even be measurable for nearby magnetars if the observations are coordinated carefully (previously only possible for neutron stars within ~100 pc, Walter & Lattimer 2002). There is a range of potential applications, not only for magnetars but also for any faint object in the Galactic plane and Galactic centre for which kinematics are scientifically interesting (e.g. Libralato et al. 2023).

Acknowledgements. We thank the referee for their report which improved the clarity and completeness of this paper. The authors also thank Nanda Rea for insightful discussions. AAC and AB acknowledge support through the European Space Agency (ESA) Research Fellowship in Space Science. JDL acknowledges support from a UK Research and Innovation Future Leaders Fellowship (grant references MR/T020784/1 and UKRI1062). NRT is supported by STFC Consolidated grant ST/W000857/1. This research is based on observations made with the NASA/ESA Hubble Space Telescope obtained from the Space Telescope Science Institute, which is operated by the Association of Universities for Research in Astronomy, Inc., under NASA contract NAS 5-26555. These observations are associated with programme 17927. This work is based in part on observations made with the NASA/ESA/CSA James Webb Space Telescope. The data were obtained from the Mikulski Archive for Space Telescopes at the Space Telescope Science Institute, which is operated by the Association of Universities for Research in Astronomy, Inc., under NASA contract NAS 5-03127 for JWST. These observations are associated with programme GO 1905. This work made use of data from the European Space Agency (ESA) mission *Gaia* (https://www.cosmos.esa.int/Gaia), processed by the *Gaia* Data Processing and Analysis Consortium (DPAC (https://www.cosmos.esa.int/web/Gaia/dpac/consortium)). Funding for the DPAC has been provided by national institutions, in particular the institutions participating in the *Gaia* Multilateral Agreement. We acknowledge use of the McGill magnetar (Olausen & Kaspi 2014), Green (Green 2025), and University of Manitoba SNRcat (Ferrand & Safi-Harb 2012) (http://snrcat.physics.umanitoba.ca) supernova remnant catalogues. This research has made use of the SVO Filter Profile Service "Carlos Rodrigo", funded by MCIN/AEI/10.13039/501100011033/ through grant PID2023-146210NB-I00 (Rodrigo et al. 2012; Rodrigo & Solano 2020; Rodrigo et al. 2024). This work made use of IPYTHON (Perez & Granger 2007), NUMPY (Harris et al. 2020), SCIPY (Virtanen et al. 2020); MATPLOTLIB (Hunter 2007), and ASTROPY (https://www.astropy.org), a community-developed core Python package for Astronomy (Astropy Collaboration 2013; Price-Whelan et al. 2018). We also used the python modules DUSTMAPS (Green 2018) and EXTINCTION (Barbary 2016).

References

Anderson, J. 2016, Empirical Models for the WFC3/IR PSF, Instrument Science Report WFC3 2016-12, 42
Anderson, G. E., Gaensler, B. M., Slane, P. O., et al. 2012, ApJ, 751, 53
Anderson, L. D., Wang, Y., Bihr, S., et al. 2017, A&A, 605, A58
Anderson, L. D., Camilo, F., Faerber, T., et al. 2025, A&A, 693, A247
Astropy Collaboration (Robitaille, T. P., et al.) 2013, A&A, 558, A33
Auchettl, K., Ng, C.-Y., Wong, B. T. T., Lopez, L., & Slane, P. 2017, ApJ, 847, 121
Bailes, M., Bassa, C. G., Bernardi, G., et al. 2021, MNRAS, 503, 5367
Barbary, K. 2016, https://doi.org/10.5281/zenodo.804967
Bedin, L. R., & Fontanive, C. 2018, MNRAS, 481, 5339
Beniamini, P., Hotokezaka, K., van der Horst, A., & Kouveliotou, C. 2019, MNRAS, 487, 1426
Blaauw, A. 1961, Bull. Astron. Inst. Netherlands, 15, 265
Blumer, H., Safi-Harb, S., Kothes, R., Rogers, A., & Gotthelf, E. V. 2019, MNRAS, 487, 5019
Bochenek, C. D., Ravi, V., Belov, K. V., et al. 2020, Nature, 587, 59
Borghese, A., & Esposito, P. 2023, in Handbook of X-ray and Gamma-ray Astrophysics, 146
Borghese, A., Rea, N., Turolla, R., et al. 2019, MNRAS, 484, 2931
Borghese, A., Coti Zelati, F., Rea, N., Esposito, P., & Israel, G. L. 2021, ATel, 14388, 1
Bower, G. C., Deller, A., Demorest, P., et al. 2015, ApJ, 798, 120
Burns, E., Svinkin, D., Hurley, K., et al. 2021, ApJ, 907, L28
Camilo, F., Ransom, S. M., Halpern, J. P., et al. 2006, Nature, 442, 892
Camilo, F., Ransom, S. M., Halpern, J. P., & Reynolds, J. 2007, ApJ, 666, L93
Camilo, F., Reynolds, J., Johnston, S., Halpern, J. P., & Ransom, S. M. 2008, ApJ, 679, 681
CHIME/FRB Collaboration (Andersen, B. C., et al.) 2020, Nature, 587, 54
Chrimes, A. A., Levan, A. J., Fruchter, A. S., et al. 2022a, MNRAS, 513, 3550
Chrimes, A. A., Levan, A. J., Fruchter, A. S., et al. 2022b, MNRAS, 512, 6093
Chrimes, A. A., Levan, A. J., Lyman, J. D., et al. 2025, A&A, 696, A127
Clark, J. S., Ritchie, B. W., Najarro, F., Langer, N., & Negueruela, I. 2014, A&A, 565, A90
Corbel, S., Chapuis, C., Dame, T. M., & Durouchoux, P. 1999, ApJ, 526, L29
Cordes, J. M., & Lazio, T. J. W. 2002, arXiv e-prints [arXiv:astro-ph/0207156]
Coti Zelati, F., Rea, N., Pons, J. A., Campana, S., & Esposito, P. 2018, MNRAS, 474, 961
Davies, B., Figer, D. F., Kudritzki, R.-P., et al. 2009, ApJ, 707, 844
de Wit, W. J., Testi, L., Palla, F., & Zinnecker, H. 2005, A&A, 437, 247
Deller, A. T., Camilo, F., Reynolds, J. E., & Halpern, J. P. 2012, ApJ, 748, L1
Dhillon, V. S., Marsh, T. R., Hulleman, F., et al. 2005, MNRAS, 363, 609
Dhillon, V. S., Marsh, T. R., Littlefair, S. P., et al. 2011, MNRAS, 416, L16

Ding, P.-J., Zhu, Z., & Liu, J.-C. 2019, Res. Astron. Astrophys., 19, 068
Ding, H., Deller, A. T., Lower, M. E., et al. 2020, MNRAS, 498, 3736
Ding, H., Lower, M. E., Deller, A. T., et al. 2024, ApJ, 971, L13
Disberg, P., & Mandel, I. 2025, ApJ, 989, L8
Disberg, P., Gaspari, N., & Levan, A. J. 2024, A&A, 687, A272
Dolphin, A. E. 2000, PASP, 112, 1383
Dolphin, A. 2016, Astrophysics Source Code Library [record ascl:1608.013]
Durant, M., & van Kerkwijk, M. H. 2005, ApJ, 627, 376
Durant, M., & van Kerkwijk, M. H. 2006a, ApJ, 650, 1070
Durant, M., & van Kerkwijk, M. H. 2006b, ApJ, 652, 576
Durant, M., & van Kerkwijk, M. H. 2006c, ApJ, 648, 534
Eikenberry, S. S., Matthews, K., LaVine, J. L., et al. 2004, ApJ, 616, 506
Eldridge, J. J., Langer, N., & Tout, C. A. 2011, MNRAS, 414, 3501
Ertan, Ü., Erkut, M. H., Ekşi, K. Y., & Alpar, M. A. 2007, ApJ, 657, 441
Espinoza, C. M., Vidal-Navarro, M., Ho, W. C. G., Deller, A., & Chatterjee, S. 2022, A&A, 659, A41
Esposito, P., Burgay, M., Possenti, A., et al. 2009, MNRAS, 399, L44
Esposito, P., Rea, N., Borghese, A., et al. 2020, ApJ, 896, L30
Esposito, P., Rea, N., & Israel, G. L. 2021, Astrophys. Space Sci. Lib., 461, 97
Fahlman, G. G., & Gregory, P. C. 1981, Nature, 293, 202
Ferrand, G., & Safi-Harb, S. 2012, Adv. Space Res., 49, 1313
Ferrario, L., & Wickramasinghe, D. 2006, MNRAS, 367, 1323
Fitzpatrick, E. L. 1999, PASP, 111, 63
Fruchter, A. S., & Hook, R. N. 2002, PASP, 114, 144
Gaia Collaboration (Vallenari, A., et al.) 2023, A&A, 674, A1
Gelfand, J. D., & Gaensler, B. M. 2007, ApJ, 667, 1111
Gençali, A. A., & Ertan, Ü. 2024, MNRAS, 534, 1481
Giacomazzo, B., & Perna, R. 2013, ApJ, 771, L26
Gilmozzi, R., & Spyromilio, J. 2007, Messenger, 127, 11
Goedhart, S., Cotton, W. D., Camilo, F., et al. 2024, MNRAS, 531, 649
Gompertz, B. P., O'Brien, P. T., & Wynn, G. A. 2014, MNRAS, 438, 240
Green, G. M. 2018, J. Open Source Softw., 3, 695
Green, D. A. 2019, JApA, 40, 36
Green, D. A. 2025, JApA, 46, 14
Guarcello, M. G., Almendros-Abad, V., Lovell, J. B., et al. 2025, A&A, 693, A120
Hamburg, R., Malacaria, C., Fletcher, C., & Fermi GBM Team. 2021, GCN, 30407, 1
Hamil, O., Stone, J. R., Urbanec, M., & Urbancová, G. 2015, Phys. Rev. D, 91, 063007
Hare, J., Pavlov, G. G., Posselt, B., et al. 2024, ApJ, 972, 176
Harris, C. R., Millman, K. J., van der Walt, S. J., et al. 2020, Nature, 585, 357
Helfand, D. J., Chatterjee, S., Brisken, W. F., et al. 2007, ApJ, 662, 1198
Hobbs, G., Lorimer, D. R., Lyne, A. G., & Kramer, M. 2005, MNRAS, 360, 974
Hu, R.-C., & Zhang, B. 2026, ApJ, 999, 102
Hulleman, F., Tennant, A. F., van Kerkwijk, M. H., et al. 2001, ApJ, 563, L49
Hulleman, F., van Kerkwijk, M. H., & Kulkarni, S. R. 2004, A&A, 416, 1037
Hunter, J. D. 2007, Comput. Sci. Eng., 9, 90
Ibrahim, A. Y., Borghese, A., Rea, N., et al. 2023, ApJ, 943, 20
Ibrahim, A. Y., Borghese, A., Coti Zelati, F., et al. 2024, ApJ, 965, 87
Igoshev, A. P. 2020, MNRAS, 494, 3663
Igoshev, A. P., Popov, S. B., & Hollerbach, R. 2021, Universe, 7, 351
Israel, G. L., Covino, S., Stella, L., et al. 2002, ApJ, 580, L143
Israel, G. L., Covino, S., Perna, R., et al. 2003, ApJ, 589, L93
Israel, G., Covino, S., Mignani, R., et al. 2005, A&A, 438, L1
Jawor, J. A., & Tauris, T. M. 2022, MNRAS, 509, 634
Kaplan, D. L., Chatterjee, S., Hales, C. A., Gaensler, B. M., & Slane, P. O. 2009, AJ, 137, 354
Kaspi, V. M., & Beloborodov, A. M. 2017, ARA&A, 55, 261
Kaspi, V. M., & Gavriil, F. P. 2003, ApJ, 596, L71
Kern, B., & Martin, C. 2002, Nature, 417, 527
Kimble, R. A., MacKenty, J. W., O'Connell, R. W., & Townsend, J. A. 2008, SPIE Conf. Ser., 7010, 70101E
Kirsten, F., Snelders, M. P., Jenkins, M., et al. 2021, Nat. Astron., 5, 414
Kirsten, F., Marcote, B., Nimmo, K., et al. 2022, Nature, 602, 585
Koralesky, B., Frail, D. A., Goss, W. M., Claussen, M. J., & Green, A. J. 1998, AJ, 116, 1323
Kosugi, G., Ogasawara, R., & Terada, H. 2005, ApJ, 623, L125
Kothes, R., & Foster, T. 2012, ApJ, 746, L4
Kouveliotou, C., Dieters, S., Strohmayer, T., et al. 1998, Nature, 393, 235
Kouveliotou, C., Strohmayer, T., Hurley, K., et al. 1999, ApJ, 510, L115
Leahy, D. A., & Tian, W. W. 2008, AJ, 135, 167
Leahy, D. A., Ranasinghe, S., & Gelowitz, M. 2020, ApJS, 248, 16
Levan, A. J., Wynn, G. A., Chapman, R., et al. 2006, MNRAS, 368, L1
Levan, A., Kouveliotou, C., & Fruchter, A. 2018, ApJ, 854, 161
Levin, L., Bailes, M., Bates, S., et al. 2010, ApJ, 721, L33
Li, B. P., Gao, Z. F., Ma, W. Q., Zhang, W. F., & Cheng, Q. 2026, ApJ, 999, 262
Libralato, M., Bellini, A., van der Marel, R. P., et al. 2023, ApJ, 950, 101
Lin, L., Kouveliotou, C., Baring, M. G., et al. 2011, ApJ, 739, 87
Lyman, J. D., Levan, A. J., Wiersema, K., et al. 2022, ApJ, 926, 121
Margalit, B., Berger, E., & Metzger, B. D. 2019, ApJ, 886, 110
Mazets, E. P., Golentskii, S. V., Ilinskii, V. N., Aptekar, R. L., & Guryan, I. A. 1979, Nature, 282, 587
Mereghetti, S., Pons, J. A., & Melatos, A. 2015, Space Sci. Rev., 191, 315
Mereghetti, S., Rigoselli, M., Salvaterra, R., et al. 2024, Nature, 629, 58
Metzger, B. D., Margalit, B., Kasen, D., & Quataert, E. 2015, MNRAS, 454, 3311
Mignani, R. P., Bagnulo, S., De Luca, A., et al. 2007, Ap&SS, 308, 203
Mori, K., Gotthelf, E. V., Zhang, S., et al. 2013, ApJ, 770, L23
Morii, M., Kawai, N., Kataoka, J., et al. 2005, Adv. Space Res., 35, 1177
Mösta, P., Ott, C. D., Radice, D., et al. 2015, Nature, 528, 376
Mukhopadhyay, M., & Kimura, S. S. 2025, ApJ, 989, L41
Muno, M. P., Clark, J. S., Crowther, P. A., et al. 2006, ApJ, 636, L41
Muñoz-Darias, T., de Ugarte Postigo, A., & Casares, J. 2016, MNRAS, 458, L114
Negro, M., Younes, G., Wadiasingh, Z., et al. 2024, Front. Astron. Space Sci., 11, 1388953
Nomoto, K., & Kondo, Y. 1991, ApJ, 367, L19
Obergaulinger, M., Janka, H. T., & Aloy, M. A. 2014, MNRAS, 445, 3169
Oke, J. B., & Gunn, J. E. 1983, ApJ, 266, 713
Olausen, S. A., & Kaspi, V. M. 2014, ApJS, 212, 6
Omand, C. M. B., & Sarin, N. 2024, MNRAS, 527, 6455
Palmer, D. M., Barthelmy, S., Gehrels, N., et al. 2005, Nature, 434, 1107
Pardo-Araujo, C., Rea, N., Ronchi, M., & Graber, V. 2026, arXiv e-prints [arXiv:2601.16159]
Penoyre, Z., Belokurov, V., & Evans, N. W. 2022, MNRAS, 513, 2437
Perez, F., & Granger, B. E. 2007, Comput. Sci. Eng., 9, 21
Piro, A. L., Giacomazzo, B., & Perna, R. 2017, ApJ, 844, L19
Ponti, G., Morris, M. R., Terrier, R., et al. 2015, MNRAS, 453, 172
Poveda, A., Ruiz, J., & Allen, C. 1967, Boletin de los Observatorios Tonantzintla y Tacubaya, 4, 86
Predehl, P., & Schmitt, J. H. M. M. 1995, A&A, 293, 889
Price-Whelan, A. M., Sipőcz, B. M., Günther, H. M., et al. 2018, AJ, 156, 123
Ranasinghe, S., & Leahy, D. 2023, ApJS, 265, 53
Rea, N., & De Grandis, D. 2026, in Encyclopedia of Astrophysics, 3, 205
Rea, N., Lo Curto, G., Testa, V., et al. 2010, MNRAS, 407, 1887
Rea, N., Gullón, M., Pons, J. A., et al. 2015, ApJ, 813, 92
Reboul-Salze, A., Guilet, J., Raynaud, R., & Bugli, M. 2022, A&A, 667, A94
Renzo, M., Zapartas, E., de Mink, S. E., et al. 2019, A&A, 624, A66
Rigoselli, M., Mereghetti, S., Halpern, J. P., Gotthelf, E. V., & Bassa, C. G. 2024, ApJ, 976, 228
Ritchie, B. W., Clark, J. S., Negueruela, I., & Langer, N. 2010, A&A, 520, A48
Rodrigo, C., & Solano, E. 2020, in XIV.0 Scientific Meeting (virtual) of the Spanish Astronomical Society, 182
Rodrigo, C., Solano, E., & Bayo, A. 2012, SVO Filter Profile Service Version 1.0, IVOA Working Draft 15 October 2012
Rodrigo, C., Cruz, P., Aguilar, J. F., et al. 2024, A&A, 689, A93
Sano, H., Suzuki, H., Nobukawa, K. K., et al. 2021, ApJ, 923, 15
Sautron, M., McEwen, A. E., Younes, G., et al. 2025, ApJ, 986, 88
Schlafly, E. F., & Finkbeiner, D. P. 2011, ApJ, 737, 103
Schneider, F. R. N., Ohlmann, S. T., Podsiadlowski, P., et al. 2019, Nature, 574, 211
Schneider, F. R. N., Ohlmann, S. T., Podsiadlowski, P., et al. 2020, MNRAS, 495, 2796
Scholz, P., Ng, C. Y., Livingstone, M. A., et al. 2012, ApJ, 761, 66
Shannon, R. M., & Johnston, S. 2013, MNRAS, 435, L29
Sharma, K., Somalwar, J., Law, C., et al. 2023, ApJ, 950, 175
Shenar, T., Wade, G. A., Marchant, P., et al. 2023, Science, 381, 761
Sherman, M. B., Ravi, V., El-Badry, K., et al. 2024, MNRAS, 531, 2379
Tam, C. R., Kaspi, V. M., van Kerkwijk, M. H., & Durant, M. 2004, ApJ, 617, L53
Tam, C. R., Gavriil, F. P., Dib, R., et al. 2008, ApJ, 677, 503
Tavani, M., Casentini, C., Ursi, A., et al. 2021, Nat. Astron., 5, 401
Taylor, A. R., Gibson, S. J., Peracaula, M., et al. 2003, AJ, 125, 3145
Tendulkar, S. P., Cameron, P. B., & Kulkarni, S. R. 2012, ApJ, 761, 76
Tendulkar, S. P., Cameron, P. B., & Kulkarni, S. R. 2013, ApJ, 772, 31
Testa, V., Rea, N., Mignani, R. P., et al. 2008, A&A, 482, 607
Testa, V., Mignani, R. P., Hummel, W., Rea, N., & Israel, G. L. 2018, MNRAS, 473, 3180
Thompson, C., & Duncan, R. C. 1993, ApJ, 408, 194
Thompson, C., & Duncan, R. C. 1995, MNRAS, 275, 255
Thompson, C., & Duncan, R. C. 1996, ApJ, 473, 322
Turolla, R., Zane, S., & Watts, A. L. 2015, Rep. Progr. Phys., 78, 116901
van Paradijs, J., Taam, R. E., & van den Heuvel, E. P. J. 1995, A&A, 299, L41
Vasiliev, E. O., Shchekinov, Y. A., & Nath, B. B. 2017, MNRAS, 468, 2757
Verberne, S., & Vink, J. 2021, MNRAS, 504, 1536

Verbunt, F., Igoshev, A., & Cator, E. 2017, A&A, 608, A57
Vink, J., & Kuiper, L. 2006, MNRAS, 370, L14
Virtanen, P., Gommers, R., Oliphant, T. E., et al. 2020, Nat. Methods, 17, 261
Walter, F. M., & Lattimer, J. M. 2002, ApJ, 576, L145
Wang, Z., Chakrabarty, D., & Kaplan, D. L. 2006, Nature, 440, 772
Weisz, D. R., Dolphin, A. E., Savino, A., et al. 2024, ApJS, 271, 47
White, C. J., Burrows, A., Coleman, M. S. B., & Vartanyan, D. 2022, ApJ, 926, 111
Woltjer, L. 1964, ApJ, 140, 1309
Woods, P. M., Kouveliotou, C., Göğüş, E., et al. 2002, ApJ, 576, 381
Yalinewich, A., Piran, T., & Sari, R. 2017, ApJ, 838, 12
Yao, J. M., Manchester, R. N., & Wang, N. 2017, ApJ, 835, 29
Younes, G., Kouveliotou, C., Jaodand, A., et al. 2017, ApJ, 847, 85
Younes, G., Baring, M. G., Kouveliotou, C., et al. 2020, ApJ, 889, L27
Zhou, P., Zhou, X., Chen, Y., et al. 2020, ApJ, 905, 99

Table A.1. Details of the *Hubble* Space Telescope observations taken under programme 17927.

Magnetar	Epoch	Filter	Start date/time [UT]	Exptime [s]	Previous epoch(s)	Filter of prev. epoch(s)	Programme ID of prev. epoch(s)
PSRJ1622(-4950)	2025.2	F125W	2025-02-28 06:26:40	1058.819	2020.7	F125W	16019
	2025.2	F160W	2025-02-28 06:47:25	1058.819	2020.7	F160W	16019
SWIFTJ1822(.3-1606)	2025.2	F125W	2025-03-30 19:53:25	1058.819	2018.5	F125W	15348
	2025.2	F160W	2025-03-30 20:14:10	1058.819	2018.5	F160W	15348
SWIFTJ1834(.9-0846)	2025.2	F125W	2025-03-30 21:27:23	1058.819	2020.2	F125W	16019
	2025.2	F160W	2025-03-30 21:48:08	1058.819	2020.2	F160W	16019
SGR1627(-41)	2025.3	F125W	2025-04-24 14:32:17	1058.819	2020.7	F125W	16019
	2025.3	F160W	2025-04-24 14:53:02	1058.819	2020.7	F160W	16019
1RXS J1708(49.0-400910)	2025.3	F125W	2025-05-06 14:17:49	1058.819	2019.8	F125W	15348
	2025.3	F160W	2025-05-06 16:13:18	1058.819	2019.8	F160W	15348
CXOUJ1714(05.7-381031)	2025.3	F125W	2025-05-06 15:52:33	1058.819	2018.3	F125W	15348
	2025.3	F160W	2025-05-06 16:13:18	1058.819	2018.3	F160W	15348
SGR1900(+14)	2025.4	F125W	2025-05-26 15:38:49	1058.819	2020.7	F125W	16019
	2025.4	F160W	2025-05-26 15:59:34	1058.819	2020.7	F160W	16019
SGR1806(-20)	2025.4	F125W	2025-06-03 18:37:11	1058.819			
	2025.4	F160W	2025-06-03 18:57:56	1058.819			
AXJ1818(.8-1559)	2025.4	F125W	2025-06-04 11:59:48	1058.819	2018.6	F125W	15348
	2025.4	F160W	2025-06-04 12:20:33	1058.819	2018.6	F160W	15348
1E2259(+586)	2025.4	F125W	2025-06-15 01:29:31	1058.819	2018.6	F125W	15348
	2025.4	F160W	2025-06-15 01:50:16	1058.819	2018.6	F160W	15348
SGR1833(-0832)	2025.5	F125W	2025-06-16 06:56:38	1058.819	2018.5	F125W	15348
	2025.5	F160W	2025-06-16 08:30:27	1058.819	2018.5	F160W	15348
SGR1935(+2154)	2025.5	F125W	2025-06-30 16:54:07	1058.819			
	2025.5	F160W	2025-06-30 17:14:52	1058.819			
					2021.4	F140W	16505
					2016.4	F140W	14502
					2015.6	F140W	14055
					2015.2	F140W	14055
SGR0501(+4516)	2025.6	F125W	2025-08-14 01:39:26	1058.819	2020.6	F125W	16019
	2025.6	F160W	2025-08-14 02:00:11	1058.819	2020.6	F160W	16019
					2012.8	F160W	12672
					2010.8	F160W	12306
4U0142(+61)	2025.5	F125W	2025-06-29 01:59:10	1058.819	2018.0	F125W	15348
	2025.5	F160W	2025-06-29 02:19:55	1058.819	2018.0	F160W	15348
CXOUJ1647(10.2-455216)	2026.1	F125W	2026-02-04 23:15:52	1058.819			
	2026.1	F160W	2026-02-04 23:29:42	1058.819			
					2023.2	F115W (JWST)	1905
					2023.2	F150W (JWST)	1905
					2023.2	F200W (JWST)	1905
					2023.2	F277W (JWST)	1905
					2023.2	F444W (JWST)	1905
					2018.4	F140W	14805
					2017.4	F140W	14805

Notes. Previous epochs of HST and/or JWST observations are listed in the last three columns. All observations use HST WFC3/IR and the F125W, F140W, or F160W NIR filters, with the exception of the JWST/NIRcam observations of CXOUJ1647. For each magnetar there is one row per filter (including observations from GO 17927 and previous programmes, where available), unless multiple epochs of imaging exist in that filter. Blank entries indicate a lack of observations in that filter either in the 2025-2026 epoch reported in this paper or in previous epochs. Shortened magnetar names are indicated in the first column, which are subsequently used throughout for brevity. Previous epoch data were published by Chrimes et al. (2022b, programme IDs 14805, 15348, and 16019), Lyman et al. (2022, programme IDs 14055, 14502, and 16505), Chrimes et al. (2025, programme IDs 12306, 12672, and 16019), Levan et al. (2018, programme IDs 14055 and 14502) and Guarcello et al. (2025, programme ID 1905). Previous epochs for SGR1806 suffered from guide star acquisition failure, resulting in unusable data.

Appendix A: Further details of the observations

A full list of the observations used in this work, and previous *Hubble* observations of the magnetars in this sample, is provided in Table A.1. An extension of Fig. 1 showing the remainder of the sample is given in Fig. A.1.

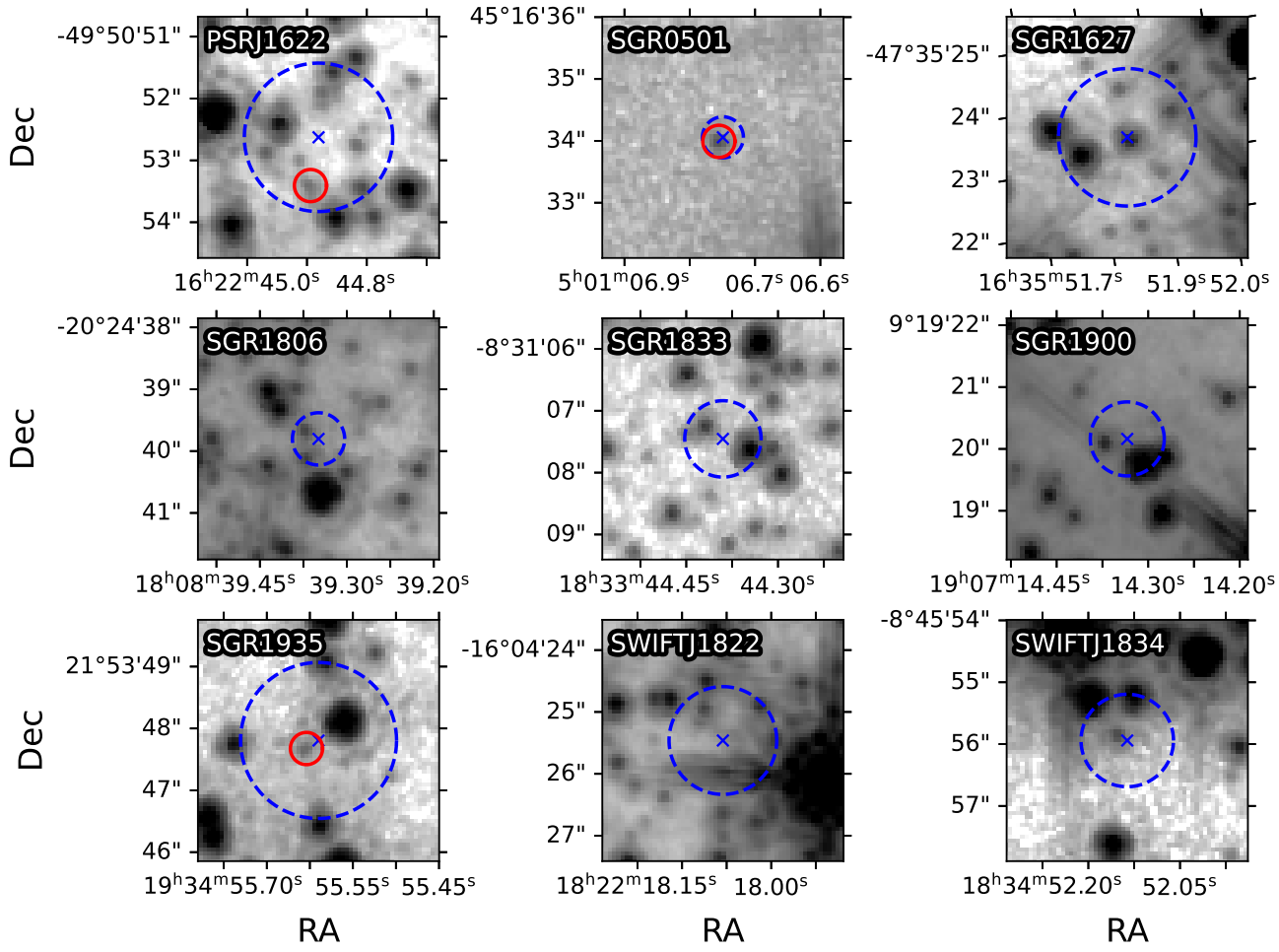


Fig. A.1. Continued from Fig. 1 in Sect. 2.

Appendix B: Full results

Additional figures showing the full results are provided in this Appendix. Figs. B.1, B.2, B.3 and B.4 are extensions to Fig. 2 showing results for the whole sample. Figure B.5 is a continuation of Fig. 4.

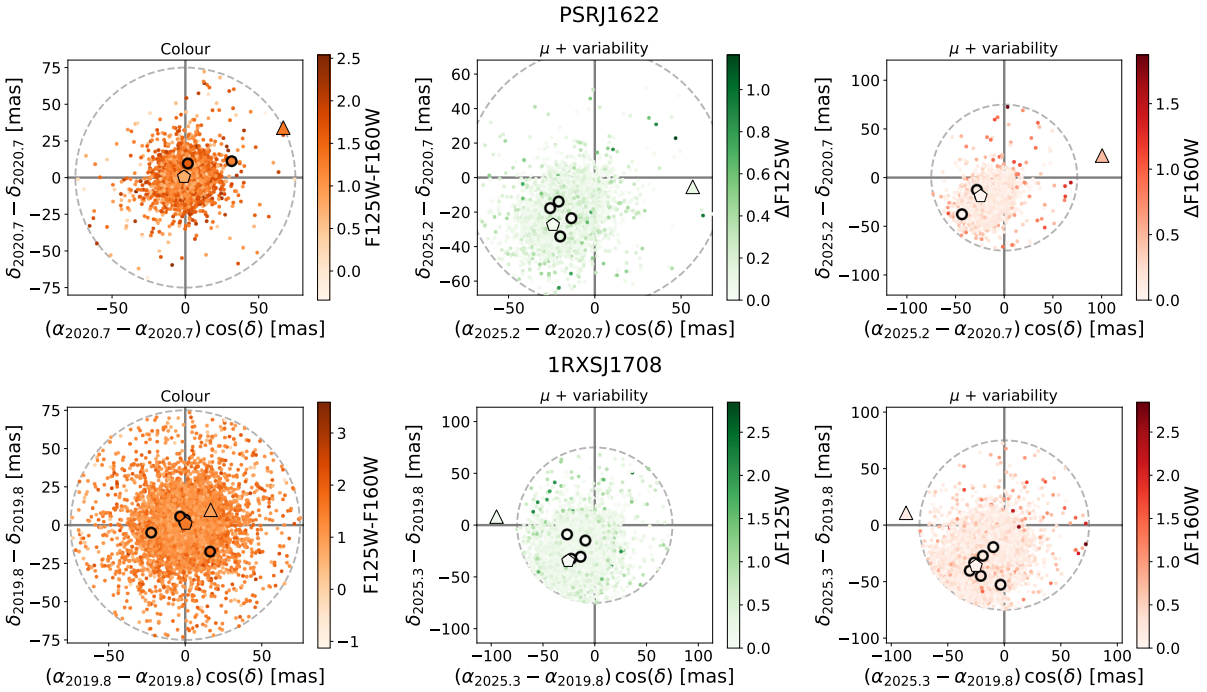


Fig. B.1. Continued from Fig. 2.

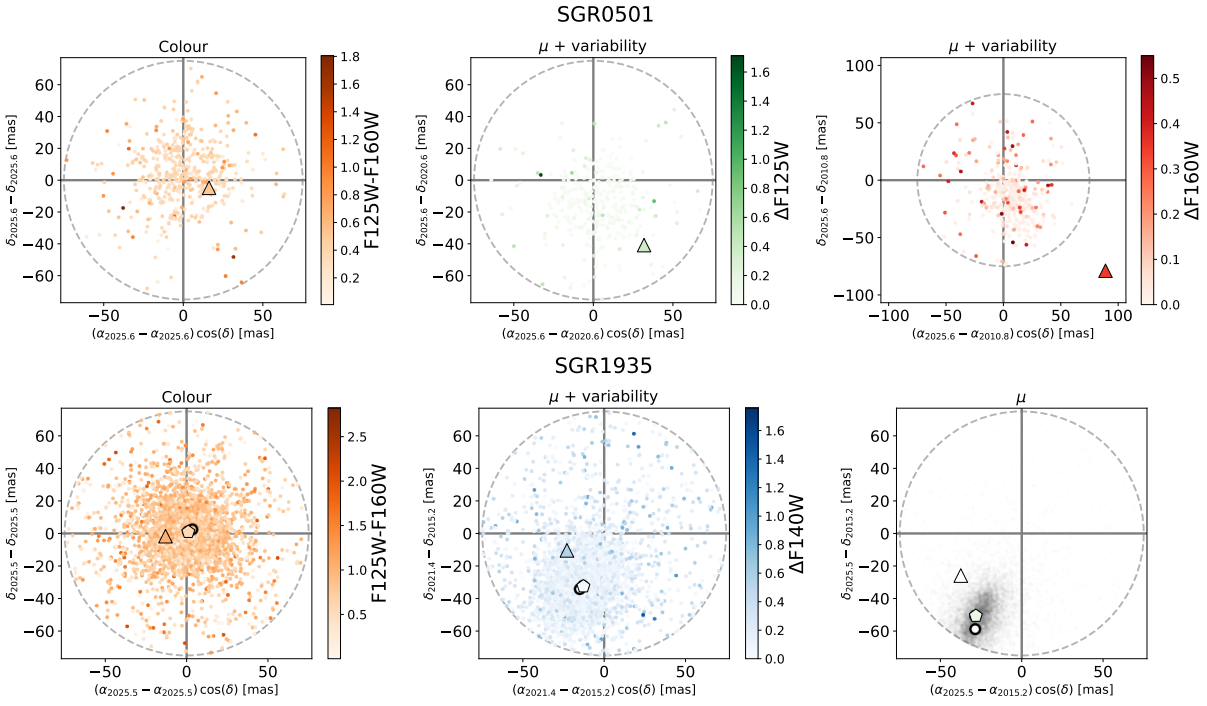


Fig. B.2. As in Figs. 2 and B.1 but for the cases where six images were available. For each filter we only show comparisons for the greatest temporal difference (e.g. 2010 vs 2025 for the F160W observations of SGR0501). The μ-only panel for SGR1935 has no colour bar, as it compares different filters at different times (F140W vs F125W). It is nevertheless included because it represents the greatest temporal baseline (and hence greatest change in RA and Dec) available for this magnetar. The lowest P_{chance} values are 0.002 (SGR0501) and 0.02 (SGR1935; this refers to the adjacent star, not the counterpart).

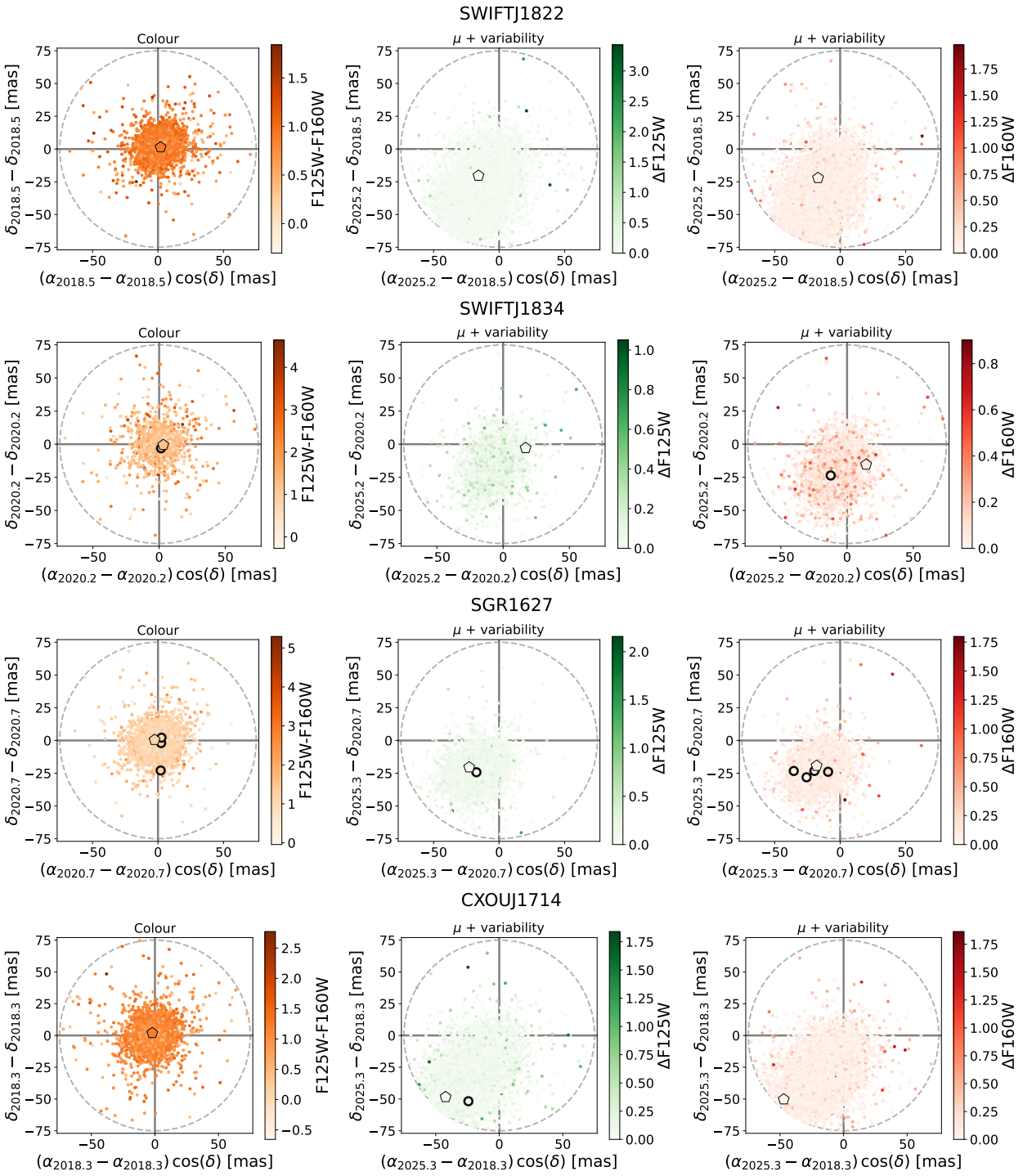


Fig. B.3. As in Figs. 2, B.1 and B.2 but for the cases where no reliable candidate was identified in the 3σ error circle based on distinct kinematics, colour, and/or variability. The sources marked with pentagons are the candidates selected solely on P_{chance} grounds by Chrimes et al. (2022b). The P_{chance} values are 0.15, 0.05, 0.03, and 0.005 (from top to bottom).

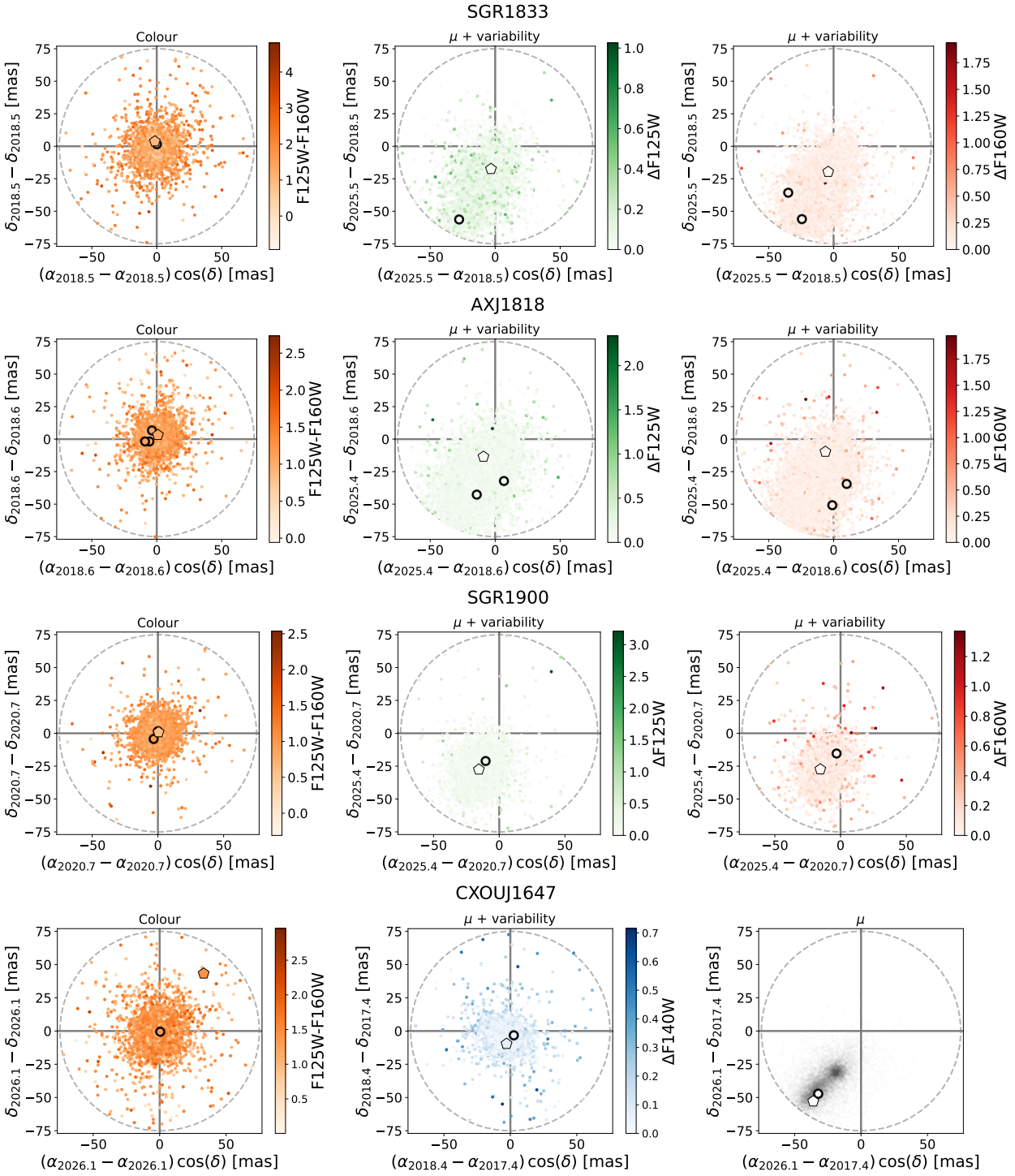


Fig. B.4. Figure B.3 continued. Additional cases where no reliable candidate was identified in the 3σ error circle based on distinct kinematics, colour, and/or variability are shown. The sources marked with pentagons are simply the candidates identified on P_{chance} grounds by Chrimes et al. (2022b). The P_{chance} values are 0.03, 0.18, 0.03, and 0.45 (from top to bottom). The last panel for CXOUJ1647 has no colour bar because it compares the first epoch in 2017 (F140W) with the JWST/NIRcam F150W image taken in 2023. Our preferred counterpart for CXOUJ1647 is not detected in the HST images and therefore does not appear in these plots.

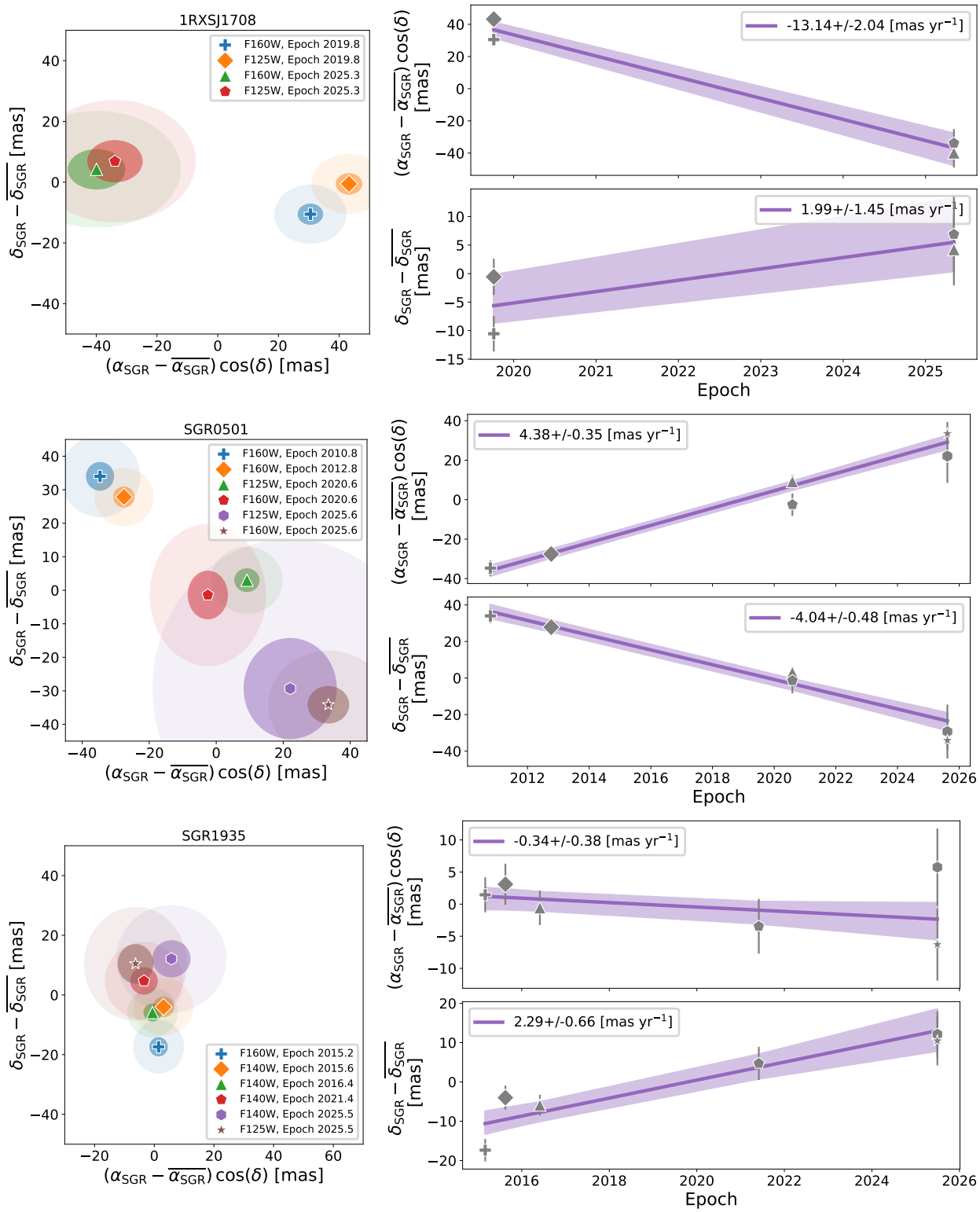


Fig. B.5. Continued as in Fig. 4 for magnetars 1RXSJ 1708, SGR0501, and SGR1935.